

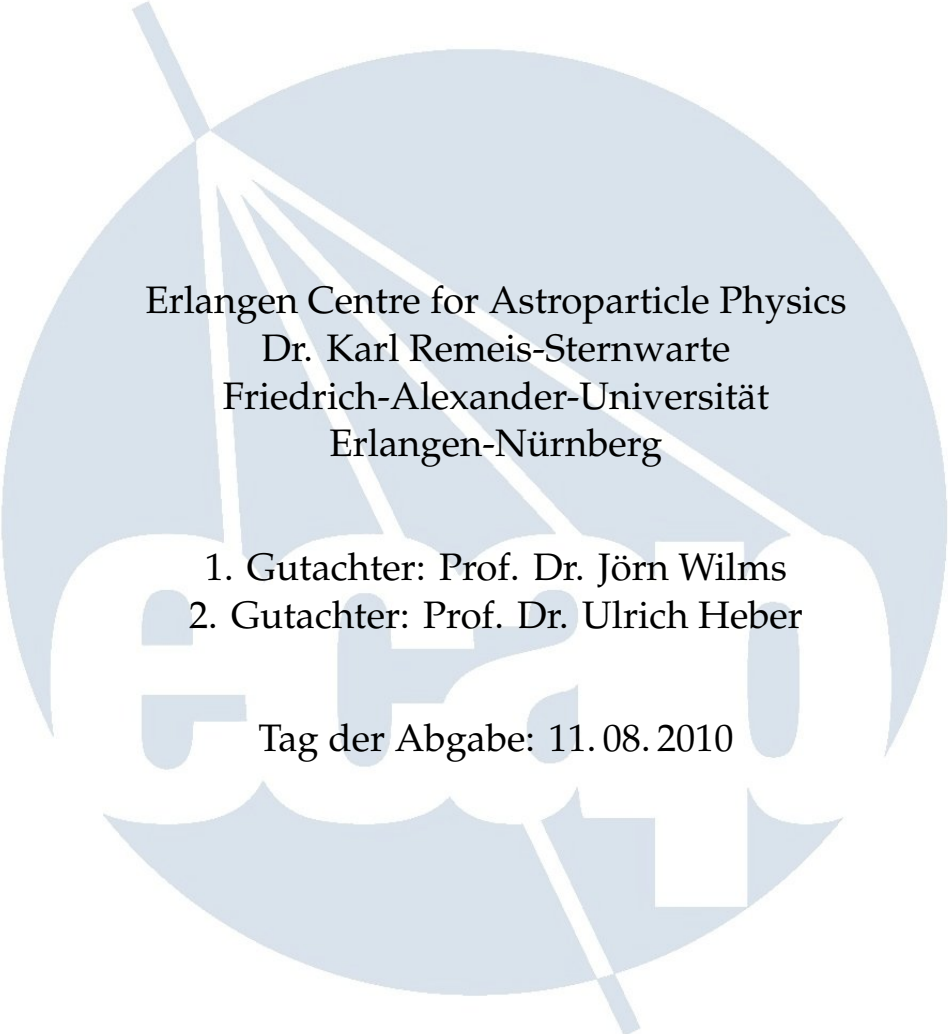
---

# Absorption dips in Cygnus X-1

---

## Bachelorarbeit

vorgelegt von  
Eckhard Strobel



Erlangen Centre for Astroparticle Physics  
Dr. Karl Remeis-Sternwarte  
Friedrich-Alexander-Universität  
Erlangen-Nürnberg

1. Gutachter: Prof. Dr. Jörn Wilms
2. Gutachter: Prof. Dr. Ulrich Heber

Tag der Abgabe: 11.08.2010



# Contents

<b>1</b>	<b>Introduction</b>	<b>4</b>
<b>2</b>	<b>Theoretical principles</b>	<b>5</b>
2.1	The <i>Rossi X-ray Timing Explorer</i> . . . . .	5
2.2	Structure in the stellar wind of hot stars . . . . .	6
2.3	Cygnus X-1 . . . . .	7
2.4	Absorption dips in Cyg X-1 . . . . .	9
<b>3</b>	<b>Analysis</b>	<b>12</b>
3.1	Data . . . . .	12
3.2	Distinction between hard and soft state . . . . .	12
3.3	Dip characterization . . . . .	14
3.3.1	Hard state events . . . . .	14
3.3.2	Soft state events . . . . .	15
<b>4</b>	<b>Results</b>	<b>18</b>
4.1	Dip distribution . . . . .	18
4.2	Testing the criterion on simulated light curves . . . . .	20
4.2.1	The Timmer & Koenig (1995) algorithm . . . . .	20
4.2.2	Correlated light curves with time lags . . . . .	22
4.2.3	Test of the criterion . . . . .	25
4.3	Stability of the dip Distribution . . . . .	26
4.4	Temporal evolution . . . . .	28
4.4.1	Measured time evolution . . . . .	28
4.4.2	Simulated time evolution . . . . .	28
4.5	Length distribution . . . . .	30
<b>5</b>	<b>Summary and outlook</b>	<b>32</b>
<b>A</b>	<b>Two sample Kolmogorov-Smirnov test</b>	<b>33</b>
<b>B</b>	<b>Inverse transform sampling</b>	<b>34</b>

# Chapter 1

## Introduction

High Mass X-ray binaries are important tools to obtain information about the structure of massive O and B stars. These binary systems consist of such a massive star and a compact object. They are, due to accretion of mass from the companion on the compact object, some of the most luminous X-ray sources in the sky. Due to the orbital motion of the two components different parts of the surrounding of the companion star are "X-rayed" by the radiation. In this way it is possible to obtain information about structures in the stellar wind of the companion stars and to test several models which describe clumps in stellar winds of massive stars (see, e.g., Feldmeier et al., 2003; Dessart & Owocki, 2005; Oskinova et al., 2007).

Cygnus X-1 is one of the most luminous X-ray sources and one of the best studied of those High Mass X-ray binaries. Its light curves show sudden decreases in the count rate during which the spectrum becomes significantly harder. These so called dips are most probable due to photoelectric absorption. Studies of the distribution of the dips with the All Sky Monitor (ASM) aboard the *Rossi X-ray Timing Explorer (RXTE)* show that they occur more often during superior conjunction of the black hole (Bałucińska-Church et al., 2000; Poutanen et al., 2008). This leads to the conclusion that there is structure in the stellar wind which is located close to the star only.

This work uses the monitoring data from pointed observations with the Proportional Counter Array (PCA) of *RXTE* with a much better time resolution to improve the statistics of the dips. A local criterion based on the hardness ratio is developed and tested to find absorption dips in the hard state automatically. To test the criterion light curves with a given PSD are simulated and a method is developed to simulate light curves with a given time lag.

With the help of the criterion a dip distribution with respect to orbital phase is obtained. It shows that dips are most frequent during superior conjunction of the black hole. In contrast to earlier investigations (see, for example, Poutanen et al., 2008; Bałucińska-Church et al., 2000) no dips are found around orbital period  $\phi \sim 0.5$  which is due to the new local criterion. Furthermore a temporal evolution is visible in the dip distribution which cannot be due a fault in the ephemeris. A Monte Carlo simulation and a Kolmogorov-Smirnov test show that it is unlikely that this development is due to statistical effects. Moreover a distribution of the dip length is measured showing that long dips are less frequent than shorter ones. Additionally no evidence is found that longer dips consist of shorter ones. All this information could be helpful for further understanding of the causes of dipping in Cyg X-1 and the structure of the stellar wind of the companion star.

# Chapter 2

## Theoretical principles

### 2.1 The *Rossi X-ray Timing Explorer*

The data used in this work were obtained from the *Rossi X-ray Timing Explorer (RXTE)* satellite. This instrument was launched on December 30, 1995 in a 580 km orbit around earth with a period of 90 min and a inclination of 23 degrees. On board of *RXTE* there are three experiments: The All Sky Monitor (ASM), the High Energy X-ray Timing Experiment (HEXTE) and the Proportional Counter Array (PCA).

The ASM consists of three wide field of view scanning detectors (Levine et al., 1996). These are able to scan most of the sky during an orbit. In this way monitoring data of all important X-ray sources is gained by taking 90 second snapshots in three different energy bands from 1.5 to 12 keV. HEXTE consists of two large areas of sodium iodide scintillators which allow measurements in the 15 to 200 keV range (Gruber et al., 1996; Rothschild et al., 1998).

The PCA contains five xenon proportional counter units (PCUs). It is sensitive in the 2 to 60 keV regime. The aim of the PCA is to measure light curves with high time resolution. It is used for pointed observation in different timing modes (for more information see Jahoda et al., 1996; Jahoda et al., 2006).

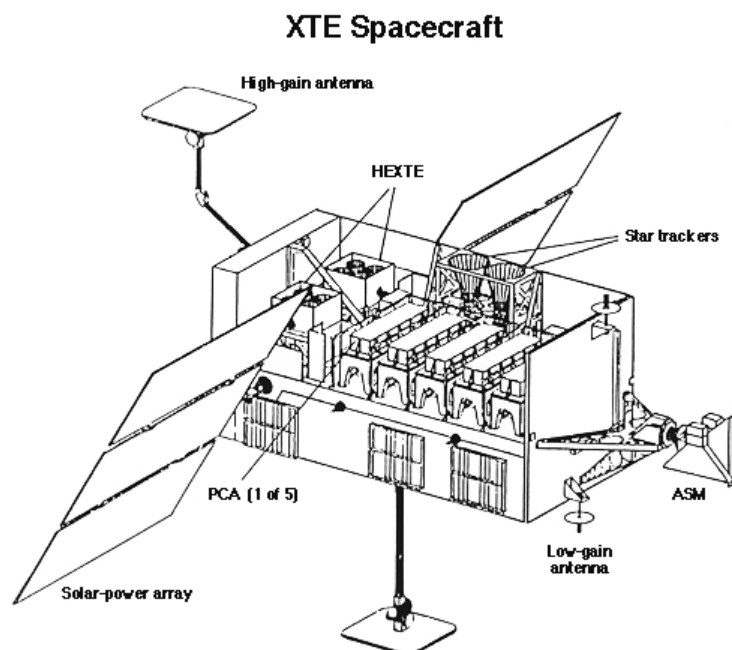


**Figure 2.1:** Schematic drawing of the *Rossi X-Ray Timing Explorer* with its three instruments ASM, HEXTE and PCA (HEASARC, <http://heasarc.gsfc.nasa.gov/Images/xte>)

## 2.2 Structure in the stellar wind of hot stars

Stellar winds of hot stars are still the subject of many studies. They are driven by resonant line scattering of the star's radiation on heavy elements (Castor et al., 1975). This process is highly unstable to radial perturbations. The so called Line-Driven-Instability leads to structure in the stellar wind, which otherwise would be thought to be homogeneous. Several models (see, e.g., Feldmeier et al., 2003; Dessart & Owocki, 2005; Oskinova et al., 2007) describe structures (called "clumps") in the stellar wind of such systems (see Fig. 2.2).

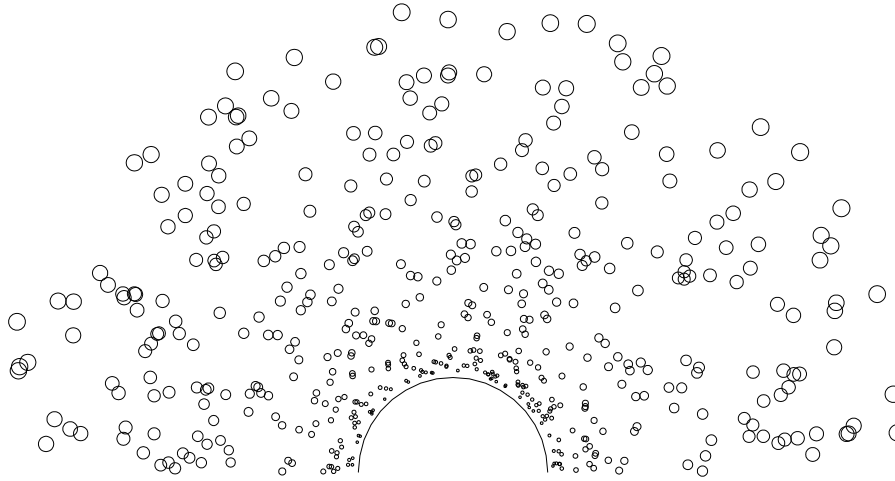


**Figure 2.2:** Expected distribution of clumps in the stellar wind of a massive star (after Oskinova et al., 2007, Fig. 1)

Various observations sustain these clumpy wind models. High mass X-ray binaries like Cyg X-1 are excellent objects to study the structure of stellar winds because of the accretion process and the orbital motion. For example Vela X-1, which consist of the B supergiant HD77581 and a neutron star, shows strong evidence for a clumpy wind through several observations.

Sako et al. (1999) fitted several wind models to line spectra out of ASCA Solid-State Imaging Spectrometer data. They found that the lines are only in accordance with the assumed mass loss rate if they introduced cool dense clumps in a hot ionized medium. These dense clumps occupy less than 5 % of the volume but contain over 90% of the mass.

Watanabe et al. (2006) derived the ionization structure of the stellar wind from *Chandra* spectra. They performed a Monte Carlo simulation for the propagation of X-ray photons through the stellar wind assuming different ionization structures. These simulations were compared to the measured spectra. They found that strong fluorescent lines from lower ionized elements, such as Fe and Mg, could be best modeled with cold dense clouds in the more highly ionized surrounding gas, which can be interpreted as clumps.

Fürst et al. (2010) draw conclusions about the accretion rate by analysing the flaring behavior of Vela X-1. They find structure in the mass accretion flow from the companion on the neutron star. These variations in the accretion rate could be linked to density variations in the stellar wind and thus to a clumpy structure. They speculate that the clump distribution is roughly log-normal. Moreover they conclude that clump sizes and masses in high mass X-ray binaries are comparable to those of supergiant fast X-ray transients.

If clumps get in between the line of sight to the X-ray emitting region, they absorb parts of the spectrum, leading to a decrease in the count rate. These events called absorption dips are observed as well in Vela X-1 (see Nagase et al., 1986) as in Cyg X-1 (see section 2.4).

## 2.3 Cygnus X-1

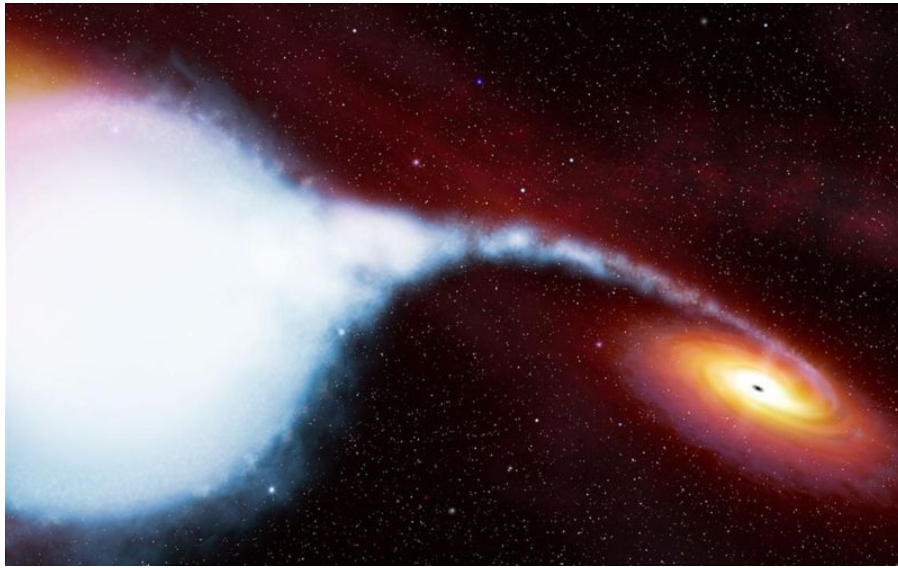


**Figure 2.3:** Artists impression of the Cygnus X-1 binary system (ESA, [http://www.spacetelescope.org/extras/posters/cygnus\\_x1/](http://www.spacetelescope.org/extras/posters/cygnus_x1/))

Cygnus X-1 is a well studied binary which consist of the supergiant HDE 226868 and a compact object. It was discovered in 1964 (Bowyer et al., 1965).

Walborn (1973) classified HDE 226868 as a O9.7Iab supergiant. The mass was determined by Herrero et al. (1995) who used unified atmospheric models also including stellar wind. They obtained a mass of  $M_* = 17.8M_{\odot}$  for HDE 226868. Because of the massive companion the binary system is a so called High Mass X-ray binary.

The mass of the compact object was calculated as  $10.1M_{\odot}$  by Herrero et al. (1995) and  $(8.7 \pm 0.8)M_{\odot}$  from Shaposhnikov & Titarchuk (2007). Most authors agree that it is above the Oppenheimer-Volkoff limit, thus Cygnus X-1 contains the first object which was believed to be a black hole.

The compact object and the companion are orbiting around each other with a period of 5.6 days. Brocksopp et al. (1999) find a modulation with this period in all wavebands. They also report of another periodicity in Cyg X-1 and attribute this superorbital period of approximately 147 days to precession and/or radiative warping of the accretion disc. Brocksopp et al. (2002) develop a model to explain the orbital modulation in the radio emission. They invoked absorption of this emission in the stellar wind of the companion to simulate light curves whose modulation is comparable to the observed one.

HDE 226868 has a strong radiation pressure driven stellar wind. This wind is focused onto the black hole due to gravitation and because the companion star is nearly filling its Roche lobe (Friend & Castor, 1982). This asymmetry of the stellar wind has to be taken into account for analysis of the wind itself. Due to orbital rotation the distance X-rays propagate through the stellar wind varies (see Fig 2.4).

This stellar wind driven accretion of mass from the companion on the compact object is the reason why Cygnus X-1 is one of the most luminous known persistent X-ray sources.

The system shows large variability over a great range of time scales. First of all there are the soft and the hard state with transitions on a monthly time scale, e.g., in 1996 May.

- The low/hard state, in which Cyg X-1 is most of the time. This state is typified by a relatively low luminosity in the soft X-rays. The spectrum above 2 keV shows a power-law with exponential cut off at approximately 150 keV.

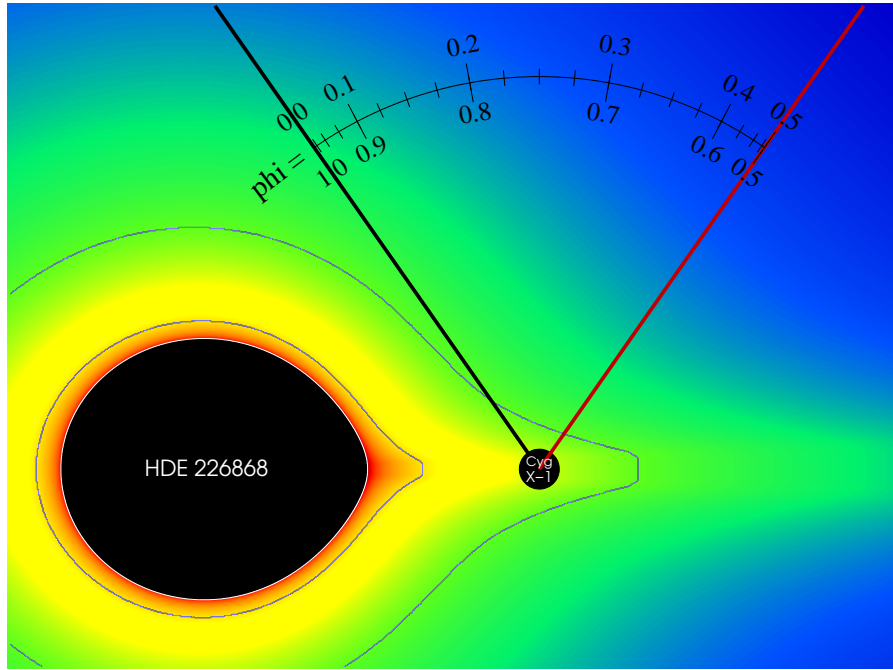


**Figure 2.4:** Density profile of the stellar wind with phase dependent line of sight from Earth (M. Hanke, priv. comm.)

- The high/soft state, in which Cyg X-1 was for approximately 34% of the time from 2000 to 2006 (Wilms et al., 2006). It is characterized by a rather high luminosity in the soft X-rays and a softer spectrum. The spectrum is dominated by thermal emission from an accretion disk

For a more intensive discussion see Remillard & McClintock (2006).

On short time scales it is also very variable. In the hard state this is due to high-frequency variability components of a Lorentzian whereas in the soft state red noise powerlaw flickering is dominant (see Pottschmidt et al., 2003, for more information).

The coherence function is a measure for the degree of linear correlation between two light curves (for a definition see Vaughan & Nowak, 1997). Pottschmidt et al. (2003) report that for Cyg X-1 in the hard state the coherence is 1 over a great range of frequencies which means that the two energy bands are fully correlated. They also state that during state transitions the coherence is dropping. The coherence in the soft state requires further investigation. Nowak et al. (1999) found a frequency dependent time lag  $\Delta\tau(f)$  between the hard and soft energy band which results in a phase shift of  $\Delta\phi = 2\pi \cdot f \cdot \Delta\tau$  between the corresponding Fourier components.



## 2.4 Absorption dips in Cyg X-1

The observed X-ray emission of Cyg X-1 sometimes shows sudden decreases (see Fig. 2.5). These events called X-ray dips were already found in early observations (e.g., by Li & Clark, 1974). Kitamoto et al. (1984) found the K-absorption-edge of iron in the spectrum of those dips and that during a dip the emitted radiation becomes harder, which means that low energies are reduced in a stronger way (see Fig. 2.6). This leads to the conclusion that dips are due to photoelectric absorption which has a larger cross-section at lower energies.

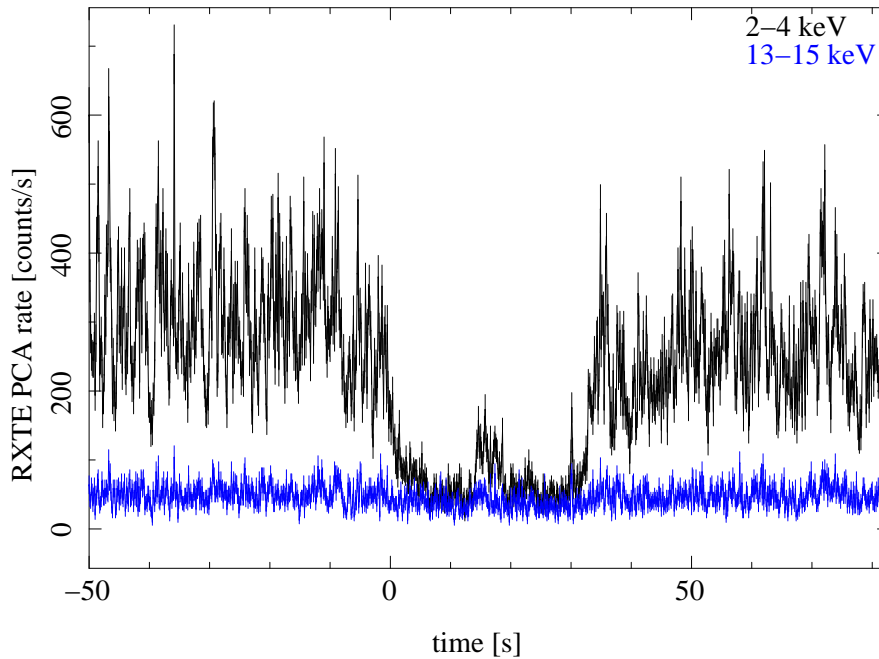


**Figure 2.5:** *RXTE*-light curve of a dip in the 2–4 keV (black) and 13–15 keV (blue) band

In addition, Bałucińska-Church et al. (1997) observed that the source flickering is reduced during the dips and that the root mean square variability amplitude is proportional to the X-ray intensity. They state that this change shows that the strong variability in the 0.7–4.0 keV band is intrinsic to the source. The observation also strengthens the hypothesis of dips being due to absorption.

First it was thought that dips occur only during or near orbital phase  $\phi = 0$ , i.e. superior conjunction of the black hole. Bałucińska-Church et al. (2000) investigated the distribution of such dips with orbital phase with the help of the *RXTE* All Sky Monitor, leading to apparently two peaks: one at orbital phase  $\phi \sim 0.95$  and one at  $\phi \sim 0.6$  (see Fig. 2.7). The latter one was attributed to an accretion stream from the companion. These authors also explained the different spectra of dips by partial covering of the source and made some connection to the stellar wind in the system.

Poutanen et al. (2008) repeated this study also using data taken after 2000. These authors did not find an indication for a peak at  $\phi \sim 0.6$  which then was claimed to be due to statistical fluctuations. They also studied the dependence of dip occurrence on the superorbital phase which allowed them to develop a model for the geometry of the system.

Feng & Cui (2002) used a full orbit observation of Cyg X-1 with *RXTE* in January 2000 to search for dips. Unlike the works presented so far they did not use spectral information (in detail the hardness ratio; see section 3.1 for a definition) to identify dips. Their criterion based only on the decrease in count rate. This results in a classification of dips. "Type A" dips, according to their nomenclature, show the same characteristics as presented so far. The spectrum hardens during the decrease in the count rate. In accordance with earlier

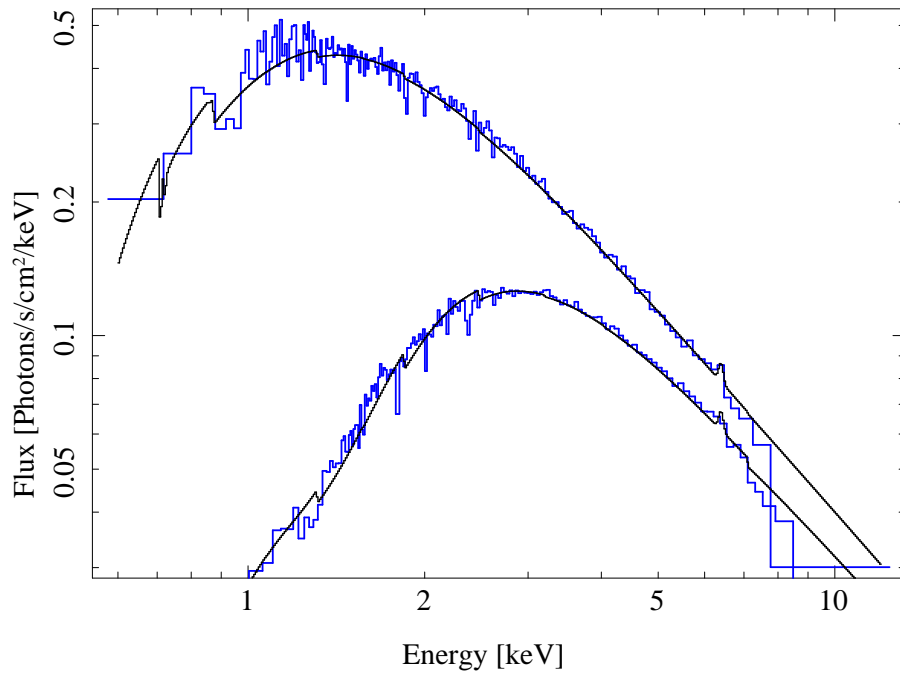


**Figure 2.6:** Chandra spectra without (upper curve) and during the dip (lower curve) (M. Hanke, priv. comm.)

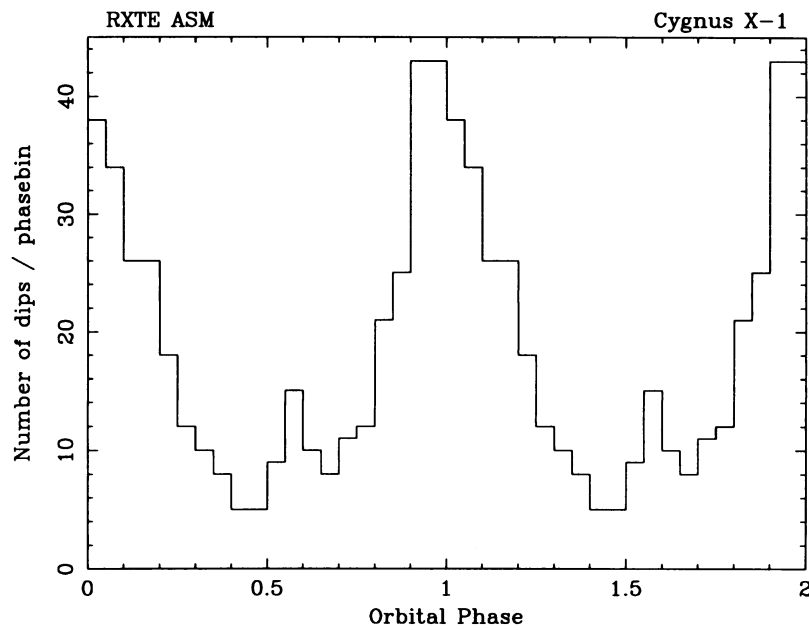


**Figure 2.7:** Distribution of dips over the orbital phase (Batucińska-Church et al., 2000, Fig. 5)

observations, these dips occur more commonly around orbital phase  $\phi = 0$ , as far as their limited statistics of 33 dips allows to infer. They also report of a new class of dips, to which they refer as "type B" dips. These show no spectral hardening and thus could not be due to photoelectric absorption. Four of their dips showed this behavior and their occurrence seemed uncorrelated to the orbital phase. They discuss the origin of these dips giving among others the following two possible explanations: On the one hand these dips could be due to partial covering of an extended source by a totally opaque medium, which they attribute to an accretion stream; on the other hand the existence of type B dips could be due to Thompson scattering of fully ionized clumps which are very close to the source.

Boroson & Vrtilek (2010) used *RXTE* ASM data to study Cyg X-1 in the soft state. They find that type A dips, which they call color dips, in the soft state depend in the same way on the orbital phase as observed beforehand. They also claim that type B dips, which they call count dips, show no dependence on orbital phase in the soft state whereas they find a dependence in the hard state.

In this work only absorption dips are discussed such that, from now on, "dip" always means "type A dip". The dependence of those dips on the orbital phase with the maximum at superior conjunction of the black hole is strong evidence for the hypothesis that dipping is connected to the wind of the companion. There are several models which try to explain the origin of the absorption dips (see, for example, Poutanen et al., 2008; Bałucińska-Church et al., 2000). A possible explanation are structures in the wind of HDE 226868. There are simulations which show clumps in the stellar wind of heavy stars (see section 2.2). In the focused stellar wind more of these clumps would be in front of the source during superior conjunction of the black hole, which can be seen in Fig 2.4. There the line of sight dependent on the orbital phase is plotted in the density profile of the stellar wind. The absorption dips in Cyg X-1 may finally allow to test such models by investigating the distribution with respect to orbital phase and the length of the dips.

# Chapter 3

## Analysis

### 3.1 Data

The data used for this work are from observations of Cyg X-1 with the PCA of the *Rossi X-ray Timing Explorer* (see section 2.1) performed between 1996 October 23 and 2010 January 14 within our monitoring campaign (Pottschmidt et al., 2003; Gleissner et al., 2004b,a; Wilms et al., 2006). Light curves were extracted at a time resolution of 0.125 s. Fig. 3.1 shows the observation time per month for the whole time span. The data were split at gaps longer than 10 min into a total number of 1531 intervals. As *RXTE* is in an orbit around Earth with a period of 90 min, most datasets therefore have an duration of approximately 50 min due to Earth occultations. The used channels can be seen in Table 3.1. The energy spans are not accurate since they changed during so called calibration epochs (see Jahoda et al., 2006). For the characterization of the dips a hardness ratio was used, which is calculated as  $(\text{rate}_5 + \text{rate}_6 + \text{rate}_7 + \text{rate}_8) / (\text{rate}_1 + \text{rate}_2)$  corresponding to (8.2 – 14.8 keV)/(2 – 5.7 keV) and from now on denoted as the hardness ratio. The energy bands were chosen such that they have approximately the same count rates and thus statistical quality in the hard state.

**Table 3.1:** Used PCA-channels and corresponding energy in PCA calibration epoch 5<sup>1</sup>

energy band	1	2	3	4	5	6	7	8
PCA channels	0-10	11-13	14-16	17-19	20-22	23-26	27-30	31-35
max energy in keV	4.5	5.7	7.0	8.2	9.5	11.1	12.8	14.8

### 3.2 Distinction between hard and soft state

As Cyg X-1 has different states (see section 2.3) it was important to categorize the data according to their state. To distinguish between hard and soft state a hardness-intensity-diagram was obtained. Therefore for each dataset a mean value of the hardness ratio is plotted against the mean value of the softest energy band. In Fig. 3.2 one can distinguish between the hard/low luminosity and the soft/high luminosity states. For the sake of simplicity the data were attributed to the soft state if the hardness ratio was smaller than 0.3. The blue parts in Fig. 3.1 show which parts of the observation satisfy this condition.

<sup>1</sup>see [http://heasarc.gsfc.nasa.gov/docs/xte/e-c\\_table.html](http://heasarc.gsfc.nasa.gov/docs/xte/e-c_table.html)

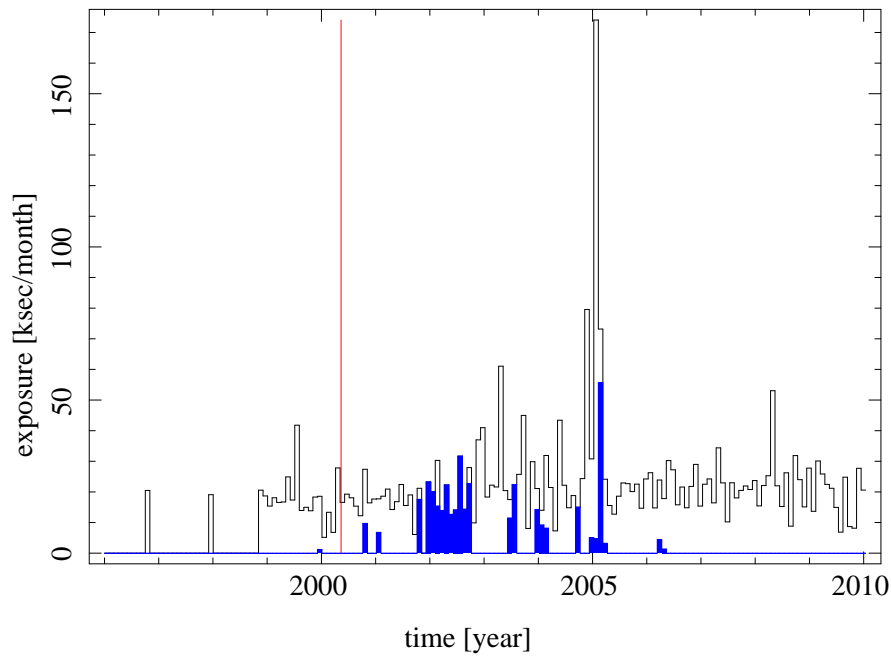


**Figure 3.1:** Monthly exposure. The blue parts correspond to the observations classified to be during a soft state. The red line shows the beginning of the PCA calibration epoch 5.

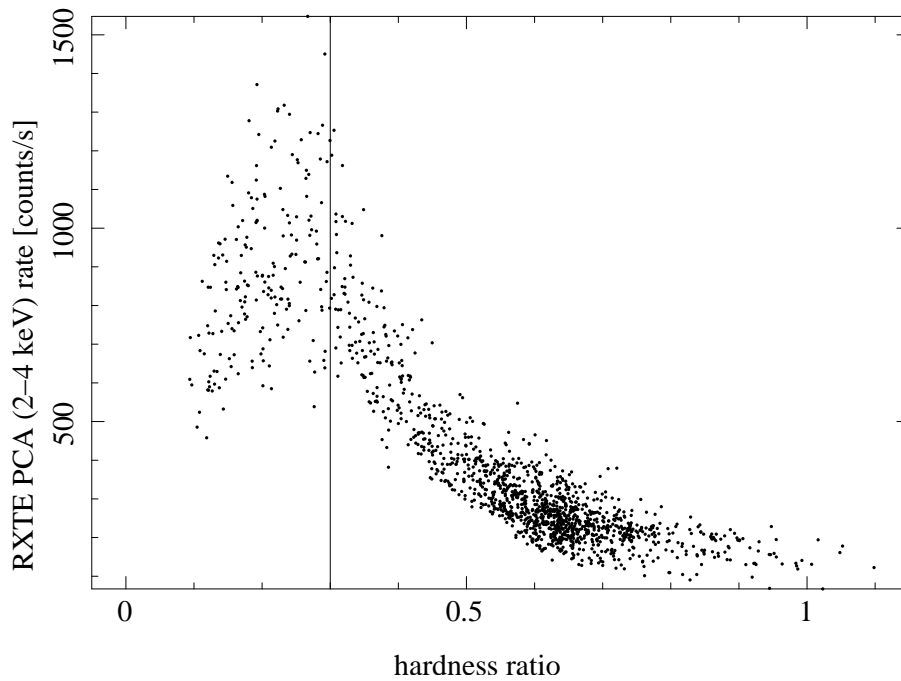


**Figure 3.2:** Hardness-intensity-diagram. The vertical line shows how soft and hard states were categorized.

### 3.3 Dip characterization

Because of the intrinsic variability of the source it is not easy to characterize dips in the light curves. To find absorption dips it is convenient to characterize dips according to an increase in the sources hardness. In previous works mostly a fixed limit for the hardness ratio was used (Bałucińska-Church et al., 2000; Poutanen et al., 2008).

Due to the intrinsic variability of the source, it seems to be more convincing to set a local criterion. Therefore the mean values  $\mu$  and standard deviation  $\sigma$  of the hardness ratio were calculated for each data set, i.e., for each continuous 50 min light curve segment.

A time span is characterized as a dipping event if its hardness ratio lies  $2\sigma$  over the mean value. To smooth out local fluctuations and so characterize the length of dips in a better way, a moving average over 7 data points (0,875s) was used instead of the hardness ratio itself. This seemed to give a more natural distinction of long dips which otherwise were sometimes split into several shorter ones. As this method still tends to characterize short, local fluctuations as dips, only structures with durations longer than 1 s were counted as dips.

#### 3.3.1 Hard state events

Fig. 3.3 shows a typical dip in the hard state. The characteristics of an absorption dip are clearly visible: The count rate in the soft energy band decreases suddenly whereas the hard one stays almost constant. The plot also shows the criterion which is used to identify the dips (i.e.,  $[\text{moving mean}(\text{HR}) - \mu]/\sigma$ ) and the hardness ratio itself.

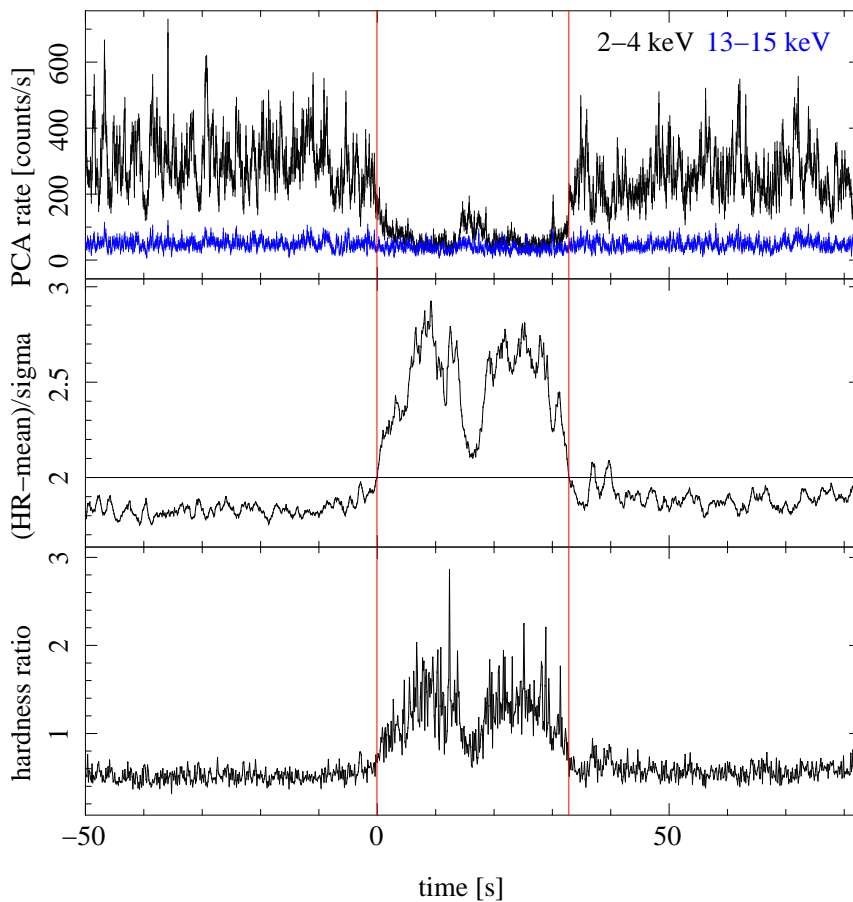


**Figure 3.3:** Typical dipping event in the hard state. Count rate in soft (2–4 keV) and hard (13–15 keV) band (top), criterion for dip selection (middle) and hardness ratio (bottom).

### 3.3.2 Soft state events

In the soft state the case is not as clear. Events that are characterized as dips by the criterion could be generally sorted in three types:

- Type A which show increase in the soft and in the hard count rate
- Type B which show an increase in the hard count rate and a decrease in the soft one
- Type C which are neither type A nor type B

Type A events (for an example see Fig. 3.4) do not show the characteristics of absorption dips. The increase in the hardness ratio shows a longer timescale trend. Moreover the count rate in both energy band is not decreasing but increasing. Almost all "dipping" events in the soft state show this correlation between count rate and hardness ratio which is typical for soft state variability. This behavior is also visible in the hardness-intensity-diagram (see Fig. 3.2).

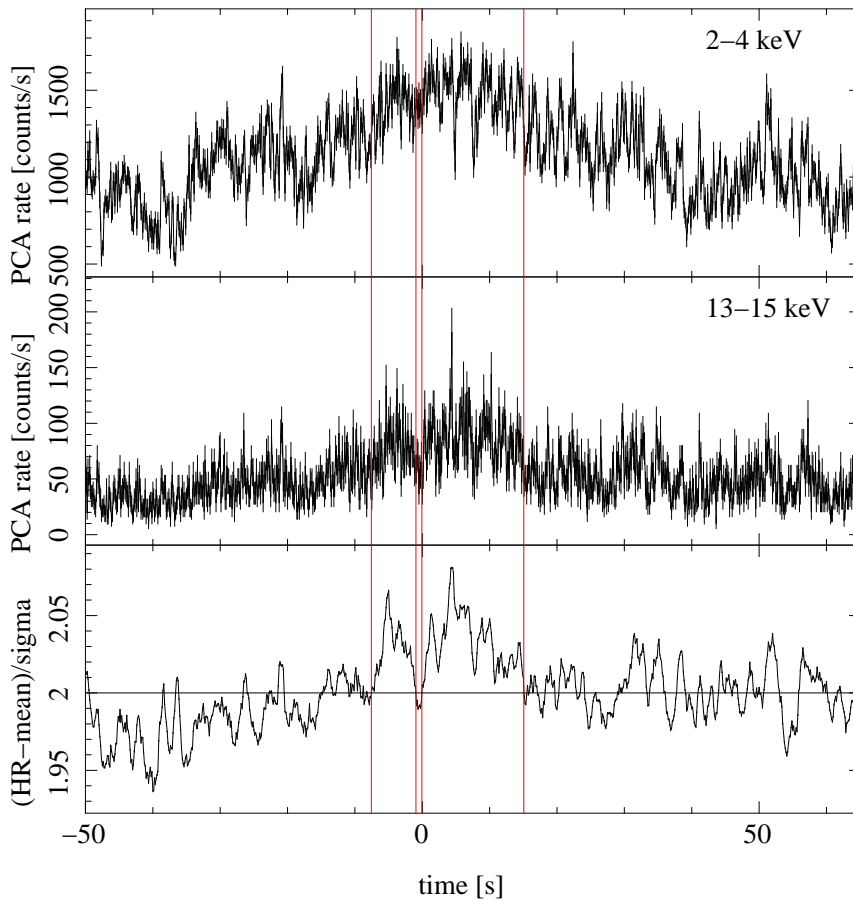


**Figure 3.4:** Typical type A event in the soft state. Count rate in soft (2–4 keV, top) and hard (13–15 keV, middle) energy band and criterion for dip selection (bottom).

Type B events (for an example see Fig. 3.5) have a decreasing count rate in the soft energy band, whereas the hard rate is increasing. This could be attributed to an overflow in the detector electronics (see, e.g., Gleissner et al., 2004b). During all of these events the soft count rate reaches the boundary luminosity and decreases subsequently. This behavior is due to the read out mechanism. If high time resolution is used, there are only a few bits of data for the count rate for each time bin. If the maximum value is reached the next one is again zero. Because of averaging over more time bins (considering a larger time resolution than the intrinsic one of this PCA mode) this overflow results in the observed behavior and not in a sudden reduction to zero in the count rate. Because of the spectral shape in the soft state it is most probable that the soft luminosity is not decreasing but increasing. This shows that Type B events may have the same physical origin as Type A ones.

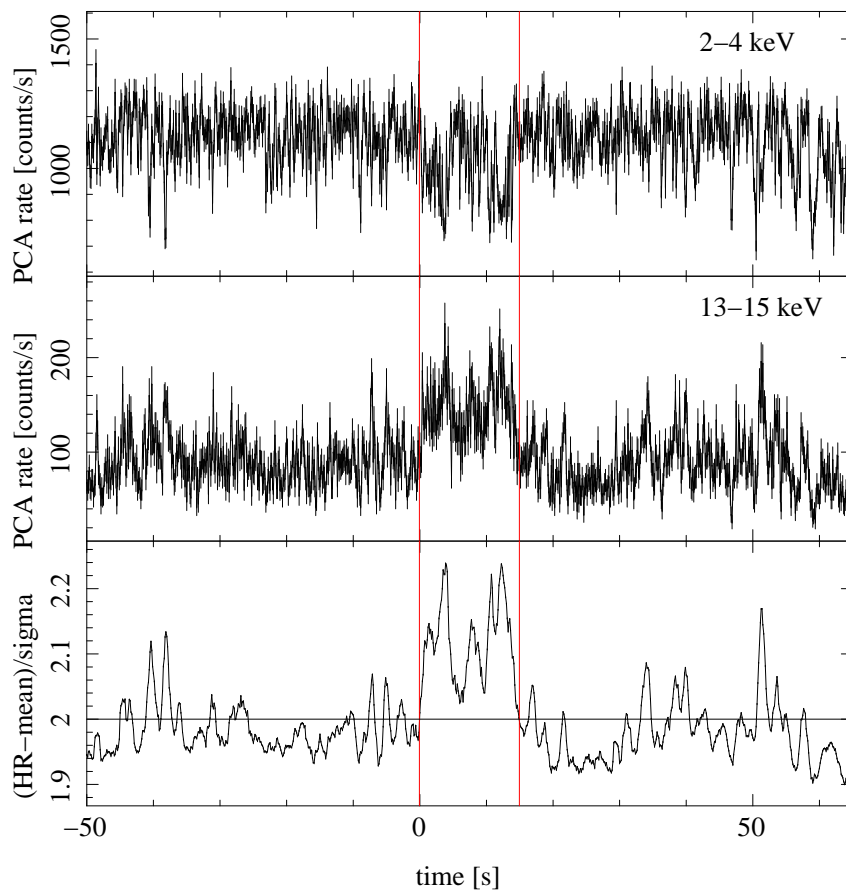


**Figure 3.5:** Typical type B event in the soft state. Count rate in soft (2–4 keV, top) and hard (13–15 keV, middle) energy band and criterion for dip selection (bottom).



Type C events (for an example see Fig. 3.6), which are characterized as not being type A/B, are more seldom but possibly show absorption dip behavior. Nevertheless the classification of type C events as absorption dips is not as clear as for the hard state because of the higher variability of the source in the soft state.

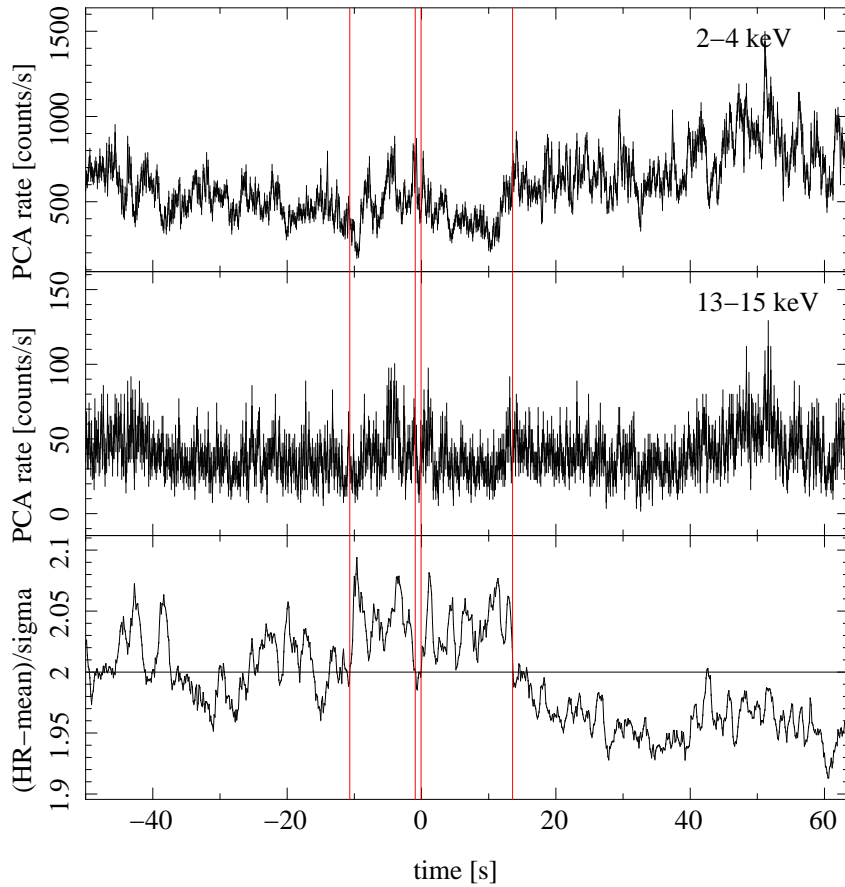


**Figure 3.6:** Typical type C event in the soft state. Count rate in soft (2–4 keV, top) and hard (13–15 keV, middle) energy band and criterion for dip selection (bottom).

To differentiate the different dips in the soft state a second criterion is set for type C events. Since type A/B share an increase in the count rate in the hard band, type C events are classified as those whose average count rate in the hard energy band during a dip is smaller than the local average.

The existence of type A and type B events as well as the diversity of type C events show that the criterion is not able to identify only absorption dips in the soft state.

# Chapter 4

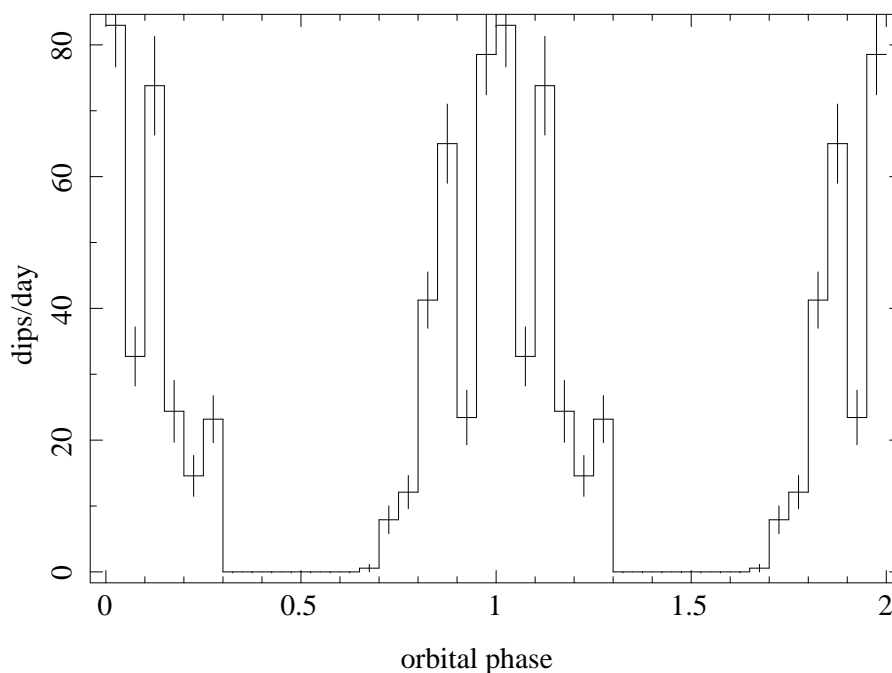
## Results

### 4.1 Dip distribution

Using the criterion described in section 3.3, 3154 dipoles were found in the whole data set. Only 857 of them were in the hard state. This is contradictory to the results of Poutanen et al. (2008) who found a larger number of dipoles in the hard state but can be understood because of their fixed threshold in the hardness ratio for dip characterization.

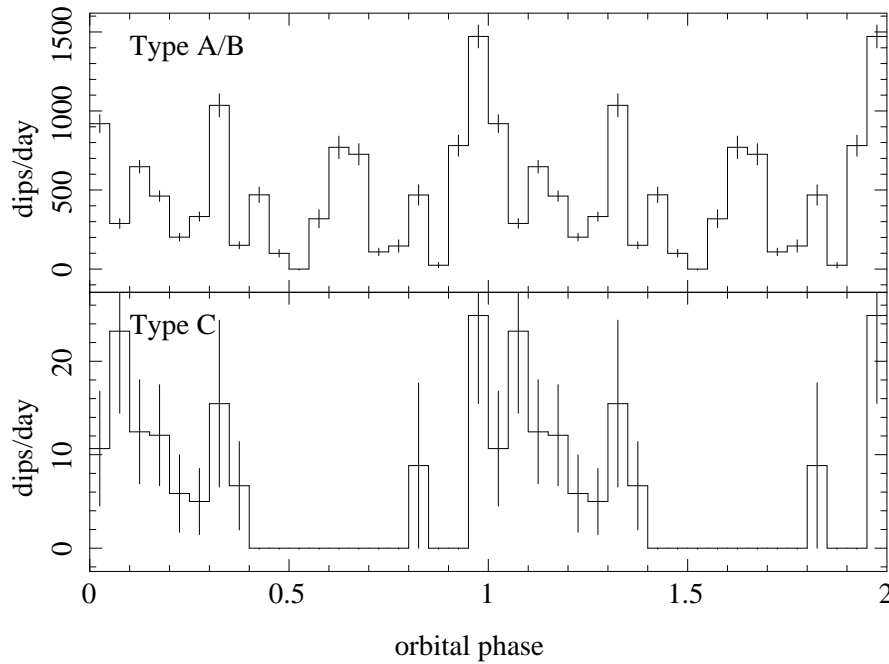
To gain a distribution of the dipoles with respect to orbital phase the orbital period was divided into 20 bins. To avoid selection effects the number of dipoles in each phase bin was normalized with the exposure in the phase bin.

Figure 4.1 shows the result for the hard state dipoles. There is a clear maximum at orbital phase  $\phi \sim 1.0$  which is consistent with the earlier observations of Bałucińska-Church et al. (2000) and Poutanen et al. (2008). The difference is that around orbital phase  $\phi \sim 0.5$  no dipoles are found at all, while the earlier investigations always seemed to find a background or even the secondary peak at  $\phi \sim 0.6$ . The reason for this difference lies in the new criterion which in contrast to the earlier ones takes local long time fluctuations into account.



**Figure 4.1:** *Distribution of the hard state dipoles over the orbit*

Figure 4.2 shows the orbital distribution of events found by the criterion in the soft state. The events are also classified with the type-scheme of section 3.3.2. It is clearly visible that the orbital dependence of type A/B events differentiates strongly from the distribution of dips in the hard state. Type C events, of which only 37 were found, show a stronger orbital dependence. Figure 4.3 shows how the hard state dips are distributed with respect to orbital phase and time. Gaps are due to soft states which could be seen in the *RXTE* ASM light curve in the bottom plot.



**Figure 4.2:** Distribution of the type A/B events and type C events over the orbit

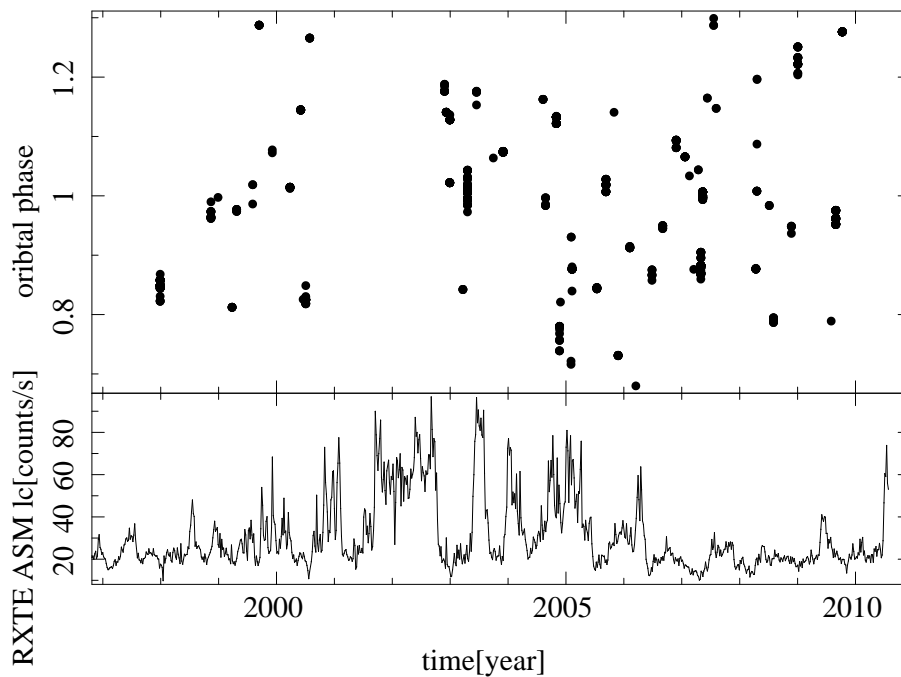


**Figure 4.3:** Distribution of the dips with respect to time and orbital phase (top) and *RXTE* ASM light curve of Cyg X-1 (bottom)

## 4.2 Testing the criterion on simulated light curves

### 4.2.1 The Timmer & Koenig (1995) algorithm

The light curves used in this section were simulated using a technique of Timmer & Koenig (1995). With the help of their algorithm it is possible to simulate normal distributed light curves of length  $T$  with a time resolution of  $t$  for a given power spectral density (PSD)  $g(f)$ . The algorithm works the following way:

1. choose the desired PSD  $g(f)$
2. calculate the Fourier frequencies  $f_i \in \left\{ \frac{1}{T}, \frac{2}{T}, \dots, \frac{1}{2t} \right\}$
3. for each  $f_i$  draw two Gaussian distributed random numbers  $y_1, y_2$  and calculate the real and imaginary part for the Fourier transform  $h(f_i) = (y_1 + iy_2) \sqrt{\frac{1}{2}g(f_i)}$
4. set the values for negative frequencies by  $h(-f_i) = h^*(f_i)$
5. perform a backward Fourier transformation of  $h(f)$  to obtain the light curve

After calculating the mean value  $\nu$  and the standard deviation  $\rho$  of the light curve  $L$  gained in this way, it can be renormalized to the desired values  $\mu$  and  $\sigma$  via the following calculation:

$$L_{new} = \mu + \frac{L - \nu}{\rho} \sigma$$

An example for a part of a simulated light curve is shown in Fig. 4.4. Fig. 4.5 shows the corresponding PSD (the one used in section 4.2.3 for the hard state simulation), which was gained out of the light curve, compared to the PSD used for the simulation.

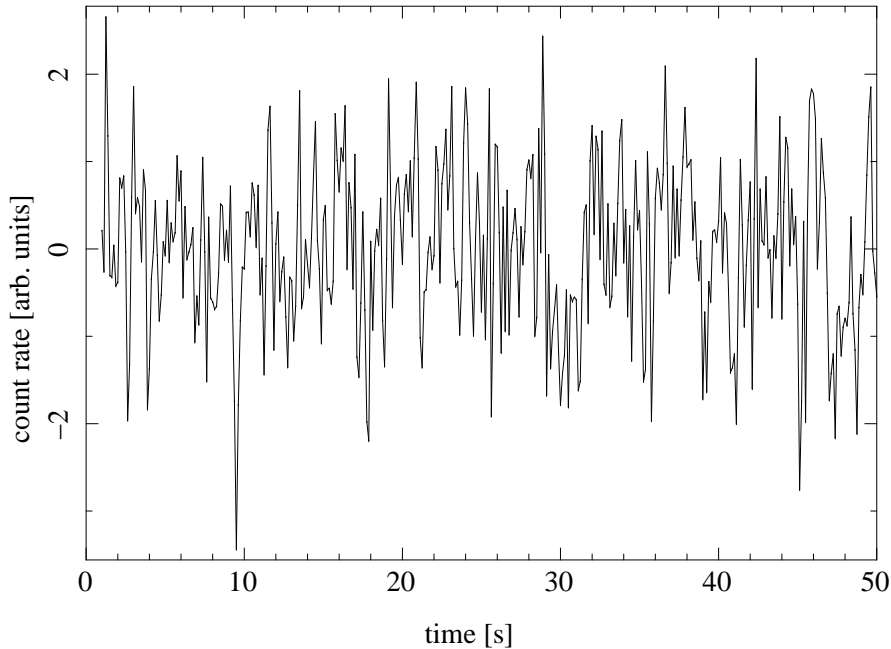


**Figure 4.4:** Part of a light curve simulated with the algorithm described above

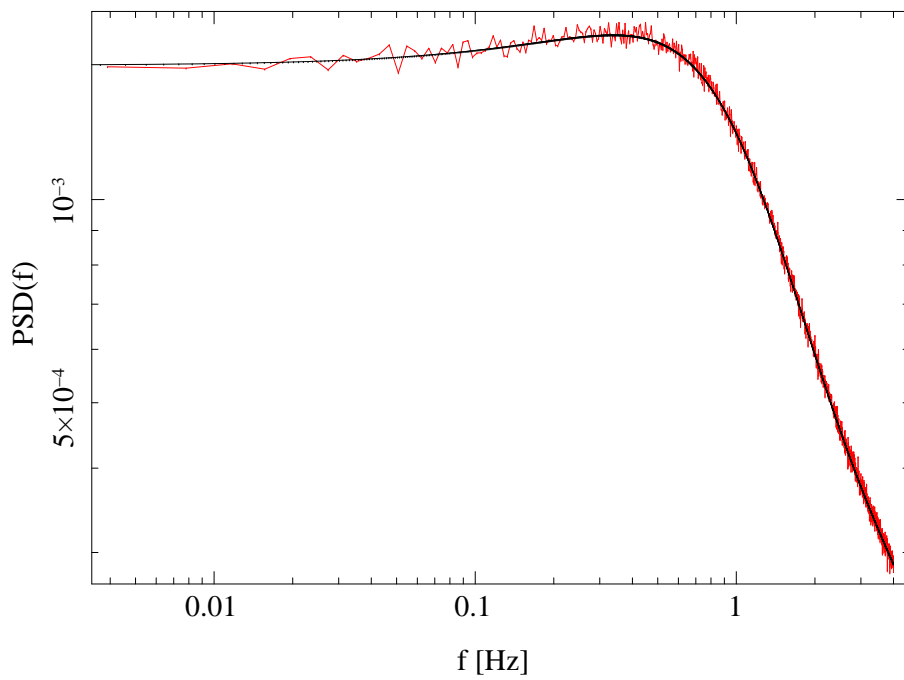


**Figure 4.5:** PSD of a simulated light curve (red) obtained by the algorithm out of the given PSD  $h(f)$  (black)

### 4.2.2 Correlated light curves with time lags

Since the different energy bands in Cygnus X-1 are correlated with each other with a time lag  $\Delta\tau(f)$  (see section 2.3) it is necessary to simulate the hard and soft energy band with this dependency. Assuming a coherence of 1 the Fourier components of the one energy band are fully determined by those of the other and the time lag spectrum. It is possible to adapt the algorithm described in section 4.2.1 to simulate two light curves in such a way.

Two light curves with a time lag of  $\Delta\tau(f)$  can be simulated if after point 3 in the algorithm a second set of Fourier components is multiplied by the phase shift in the following way

$$s(f) = h(f) \cdot \exp(2\pi i \cdot f \cdot \Delta\tau)$$

and then  $s(f)$  is treated in the same way as  $h(f)$ . Figure 4.6 shows the results of using this method for a constant time lag of  $\Delta\tau(f) = 1$  s.

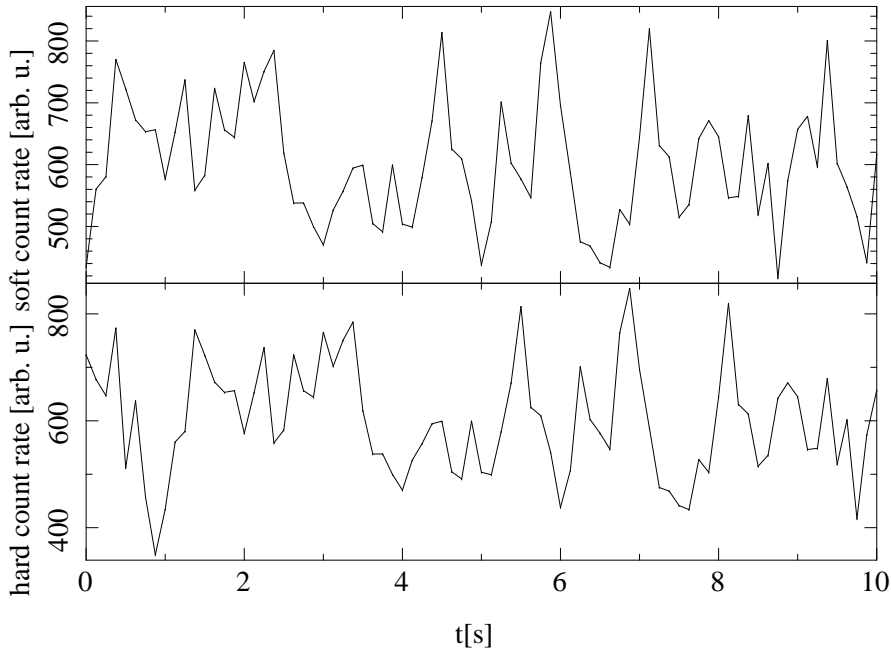


**Figure 4.6:** Two light curves simulated with a constant time lag of  $\Delta\tau(f) = 1$  s

Nowak et al. (1999) report that the measured time lags have uncertainties which are connected to Poisson noise of the detector. Therefore the each value of the light curves which were simulated in the way described above is subsequently replaced by a random number drawn out of Poisson distribution with the mean of the value. If the light curves beforehand are distributed according to the distribution  $P_{\sigma,\mu}$  with the mean value  $\mu$  and the standard deviation  $\sigma$  the new light curves are distributed according to

$$\tilde{P}_{\tilde{\sigma},\tilde{\mu}}(n) = \int_0^{\infty} dr P_{\sigma,\mu}(r) \cdot P_{\lambda=r}(n),$$

where  $P_{\lambda}$  is the Poisson distribution with mean value  $\lambda$ . Fig. 4.7 shows  $\tilde{P}_{\tilde{\sigma},\tilde{\mu}}(n)$  for the Gaussian distribution  $P_{\sigma=10,\mu=50}(n)$  as well as  $P_{\sigma=10,\mu=50}(n)$  itself.

The mean value of the new distribution can be derived using Fubini's Theorem

$$\tilde{\mu} = \int_0^{\infty} dn \tilde{P}_{\tilde{\sigma},\tilde{\mu}}(n) \cdot n = \int_0^{\infty} dr P_{\sigma,\mu}(r) \int_0^{\infty} dn P_r(n) \cdot n = \int_0^{\infty} dr P_{\sigma,\mu}(r) \cdot r = \mu$$

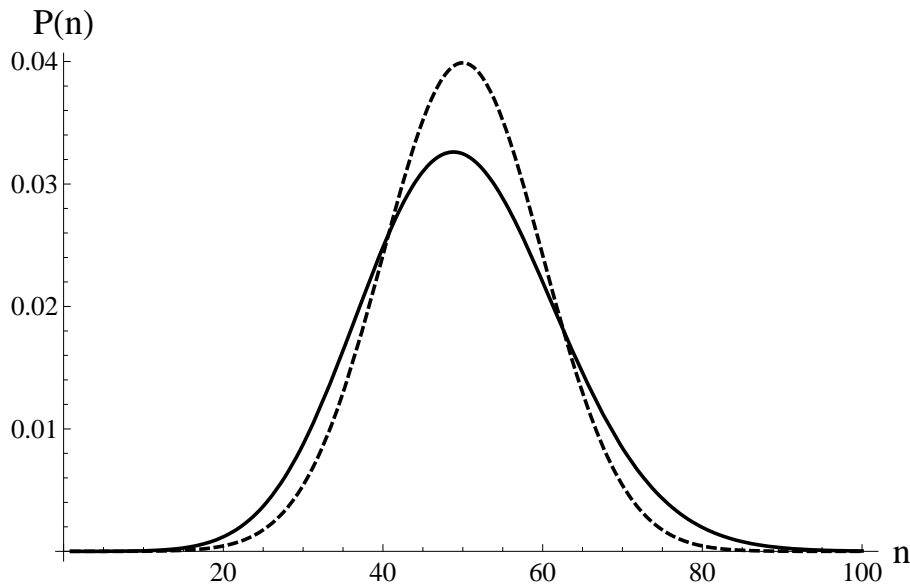


**Figure 4.7:** The Gaussian distribution  $P_{\sigma=10, \mu=50}(n)$  (dotted) and the resulting  $\tilde{P}_{\tilde{\sigma}, \tilde{\mu}}(n)$  (solid)

In the same way  $\tilde{\sigma}$  is gained using  $\tilde{\mu} = \mu$  and that the standard deviation of the Poisson distribution is  $\sqrt{\lambda}$ .

$$\begin{aligned}
 \tilde{\sigma}^2 &= \int_0^{\infty} dn \tilde{P}_{\tilde{\sigma}, \tilde{\mu}}(n) \cdot (n - \tilde{\mu})^2 = \int_0^{\infty} dr P_{\sigma, \mu}(r) \int_0^{\infty} dn P_{\lambda=r}(n) \cdot (n - \mu)^2 \\
 &= \int_0^{\infty} dr P_{\sigma, \mu}(r) \left[ \int_0^{\infty} dn P_r(n) \cdot (n - r)^2 - 2(\mu - r) \int_0^{\infty} dn P_r(n) \cdot n + (\mu^2 - r^2) \int_0^{\infty} dn P_r(n) \right] \\
 &= \int_0^{\infty} dr P_{\sigma, \mu}(r) \left[ r - 2(\mu - r) \cdot r + (\mu^2 - r^2) \right] = \int_0^{\infty} dr P_{\sigma, \mu}(r) \left[ (r - \mu)^2 + r \right] \\
 \tilde{\sigma}^2 &= \sigma^2 + \mu
 \end{aligned}$$

With the help of these relations it is possible to simulate light curves with desired mean  $\tilde{\mu}$  and standard deviation  $\tilde{\sigma}$  by setting the values to  $\mu = \tilde{\mu}$  and  $\sigma = \sqrt{\tilde{\sigma}^2 - \tilde{\mu}}$  in the way described in section 4.2.1 before applying the Poisson noise.

It is common that light curves are given in units of counts per second. Nevertheless the Poisson statistics should be applied to the measured number of counts in each time bin. This value is obtained by multiplying with the time resolution before applying the Poisson noise. By dividing it by the time resolution afterwards the result has units of counts per second and the right Poisson statistics. If the count rate should be normalized to the number of PCUs used, the same should be done with the number of PCUs. This is, for example, necessary if the mean and standard deviation are calculated out of rate per PCU data.

It is possible to simulate two light curves which follow a given PSD with a given time lag and Poisson noise in the way described above. Figure 4.8 shows the result of such a simulation for frequency dependent time lag of  $\Delta\tau(f) = 0.01 \text{ s} \cdot (f/\text{Hz})^{-0.7}$  which was used for the simulations in section 4.2.3. Timing analysis shows that such simulated light curves have the desired time lag spectrum (see Fig. 4.9).

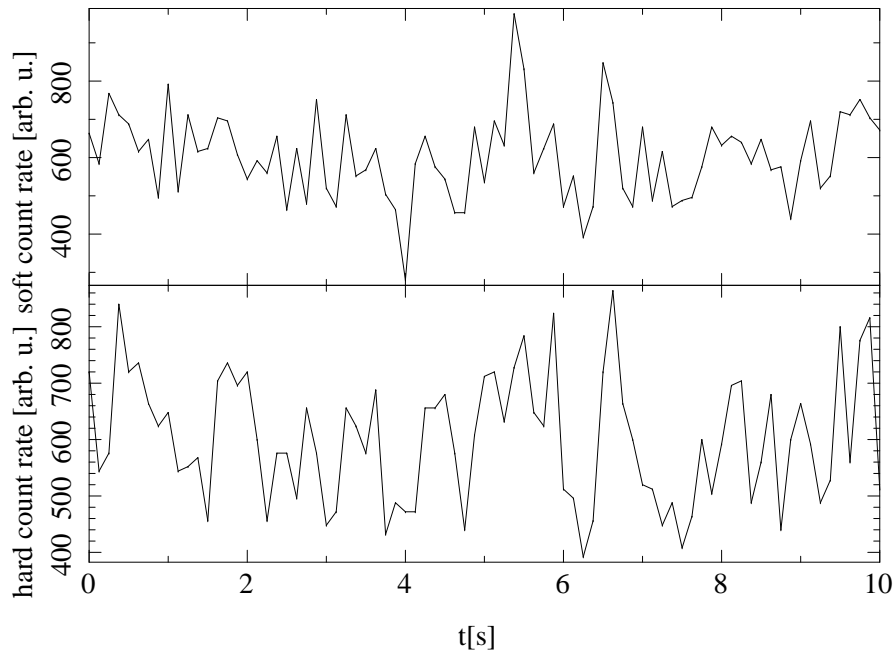


**Figure 4.8:** Two light curves simulated with a frequency dependent time lag of  $\Delta\tau(f) = 0.01 \text{ s} \cdot (f/\text{Hz})^{-0.7}$  and Poisson noise

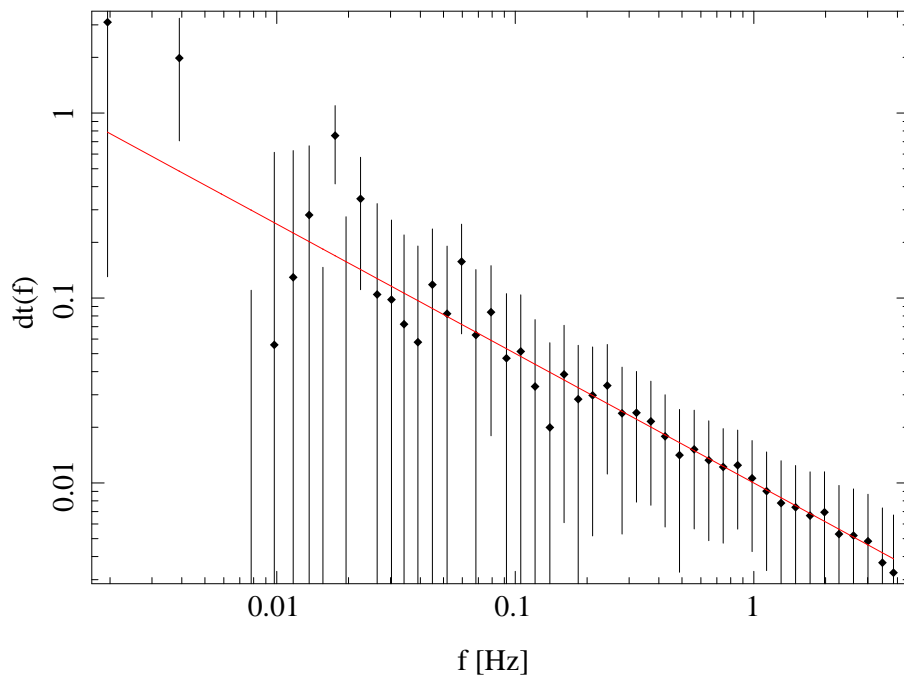


**Figure 4.9:** Time lag spectrum gained via timing analysis out of the simulated light curves (black) and time lag used for the simulation (red) (V. Grindberg, priv. comm.)



### 4.2.3 Test of the criterion

To check whether the chosen criterion is sensitive only on dipping and not also on intrinsic source variability it is tested on simulated light curves. Therefore the methods described in section 4.2.1 and 4.2.2 were used to simulate light curves with a given power spectral density. For the hard state the double Lorentzian profile

$$\text{PSD}_h(f) = \frac{2\sigma_1^2 \cdot Q_1 \cdot f_1}{\frac{\pi}{2} + \arctan(2Q_1)} \cdot \frac{1}{f_1^2 + Q_1^2 \cdot (f - f_1)^2} + \frac{2\sigma_2^2 \cdot Q_2 \cdot f_2}{\frac{\pi}{2} + \arctan(2Q_2)} \cdot \frac{1}{f_2^2 + Q_2^2 \cdot (f - f_2)^2}$$

was used as power spectral density (PSD), whereas the PSD for the soft state was chosen the a cut-off power law with Lorentz

$$\text{PSD}_s(f) = N \cdot f^\beta e^{-f/c} + \frac{2\sigma_3^2 \cdot Q_3 \cdot f_3}{\frac{\pi}{2} + \arctan(2Q_3)} \cdot \frac{1}{f_3^2 + Q_3^2 \cdot (f - f_3)^2}.$$

The parameters were obtained by a fit to typical PSDs (M. Böck, priv. comm.), see Table 4.1. Both PSDs are plotted in Fig. 4.10

**Table 4.1:** PSD parameters used for the simulation of light curves

parameter	$\sigma_1$	$f_1$ [Hz]	$Q_1$	$\sigma_2$	$f_2$ [Hz]	$Q_2$
value	0.0408405	0.588488	0.3437823	0.03840426	4.382007	0.3950863
parameter	$N$	$\beta$	$c$ [Hz]	$\sigma_3$	$f_3$ [Hz]	$Q_3$
value	0.001083116	1	30	0.02537187	3.245546	0.3860634

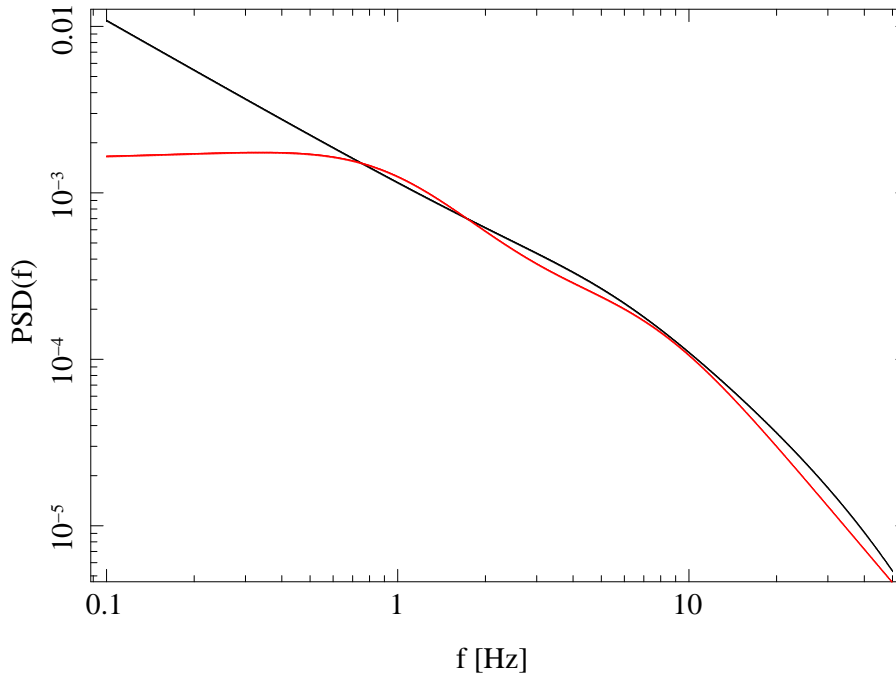


**Figure 4.10:** PSDs used for the simulations in the hard state (red) and in the soft state (black)

For each observation orbit a light curve is simulated for the hard and soft energy band with the corresponding mean and standard deviation and the respective PSD. The length of each

of these light curves is chosen as  $2^{15} \text{ s} \approx 9 \text{ h}$  such that it is at least 10 times longer than the real observations.

An important fact is that the light curves for the hard and soft energy band are correlated (see section 2.3). Assuming a coherence of 1 and that the errors in the time lag are only due to noise in the detector the algorithm of Timmer & Koenig (1995) could be adapted to simulate light curves for the soft and hard energy band with a given time lag (see section 4.2.2). Since the coherence is not 1 in transitional states and there is no information about the soft state, such a simulation should be seen as a boundary case of fully correlated energy bands. Simulations with two fully uncorrelated energy bands are the other boundary case. For uncorrelated light curves in the hard state simulation 185 dips were found by the criterion. Taking into account that the simulated light curves are longer this results in a total number of approximately 11.4 simulated dips for the real hard state observation times. In the soft state 24242 dips were found resulting in a total of 1494.7 dips for the soft state observation time.

Using a frequency dependent time lag of  $\Delta\tau(f) = 0.01 \text{ s} \cdot (f/\text{Hz})^{-0.7}$  (which was estimated out of Nowak et al., 1999) no dips were found in the hard state. In the soft state 13231 dips were found and this results in 808.6 for the soft state observation time. This shows that the correlation make false-dips more unlikely to happen, because local fluctuations in the hardness are less probable with correlated light curves.

Both cases show that in the hard state the criterion could be trusted to find absorption dips while in the soft state this is probably not the case. Therefore only hard state dipping events are discussed in this work from now on.

### 4.3 Stability of the dip Distribution

To test the statistical stability of the dip distribution, several subsets of the data were taken and compared. Fig. 4.11 shows the distribution subsets of even and odd observation numbers, while Fig. 4.12 shows the first and second half of the whole campaign.

To check stability a two sample Kolmogorov-Smirnov test was performed (see appendix A). The null hypothesis is that the cumulative distribution functions  $F_1$  and  $F_2$  two empiric samples consisting of  $n_1$  and  $n_2$  observations are distributed according to the same distribution. It is rejected at level  $\alpha$  if  $D > D_{n_1, n_2, \alpha}$  is valid for the test statistic

$$D = \max \{|F_1(x) - F_2(x)|\}.$$

With  $n_1 = n_2 = 428$  and for  $\alpha = 0.01$  we obtain  $D_{428, 428, 0.01} = 0.111$ .

For the first division where every second observation was separated,  $D$  was obtained as  $D = 0.002$  such that at the 1% level the null hypothesis is not rejected. This shows the statistical stability of the data.

In contrast to that, the second subsets where the data were split temporally, have  $D = 0.228$ . This value is greater than the limit  $D_{428, 428, 0.01} = 0.111$  such that the null hypothesis is rejected at the 1% level. This leads to the conclusion that the dip distribution evolves with time as the first and the second time span of the observation are most probably not from the same distribution.

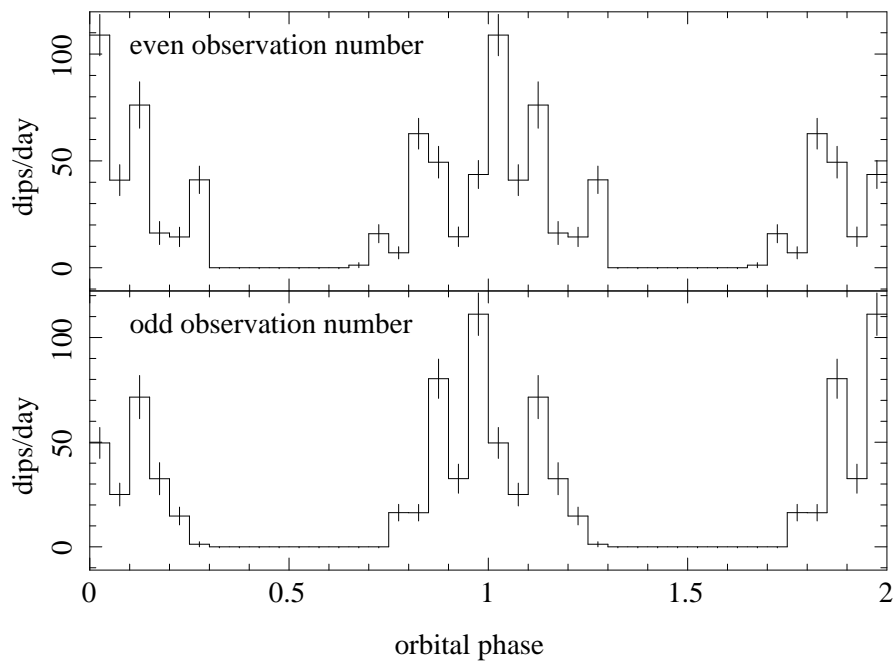


**Figure 4.11:** Subsets of the dip distribution using every other dataset

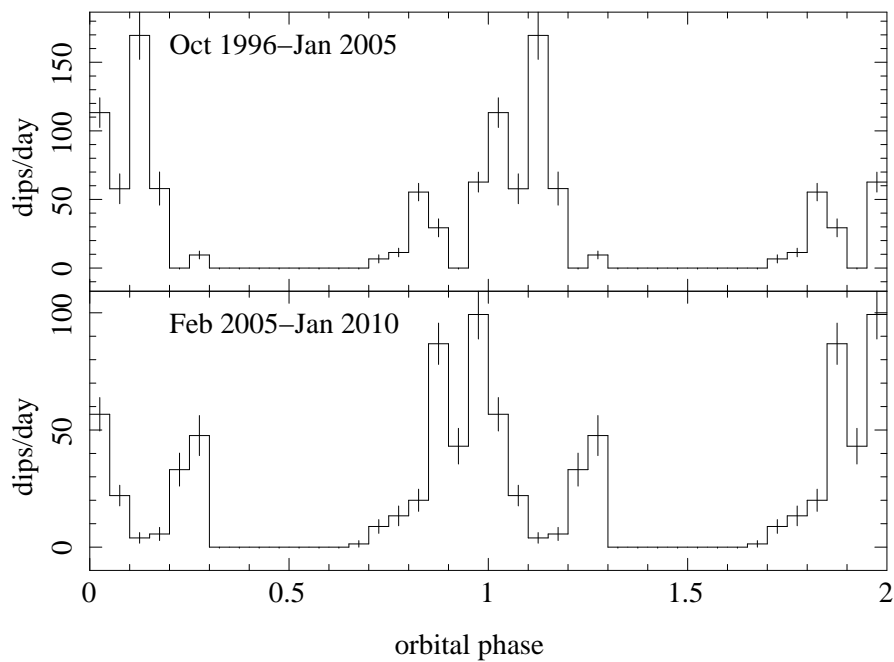


**Figure 4.12:** Subsets of the dip distribution using the first and second half of the campaign

## 4.4 Temporal evolution

### 4.4.1 Measured time evolution

The evolution of the dip distribution in time was examined further by dividing the observations into smaller bits. This is only possible to certain minimal size for a subset because the statistic is affected if the number of observations in one of the phase bins reaches zero. Choosing a time interval of two years this happens only twice in bins where no dip are found in the whole time span. To see a temporal trend it is important that the subsets are connected. Because of the long soft state in 2002 there would be a disconnection such that all data before are excluded in this section. The time evolution of the center of the dip distribution of the remaining data is shown in Fig. 4.13. For every time the average of the dip distribution of a timespan beginning one year in the future and ending one year in the past is plotted. The center of the dip distribution is clearly shifting in time. This could be due to real temporal evolution or statistical effects. It is unlikely that this is due to faults in the ephemeris because this would only result in shifting into one direction.

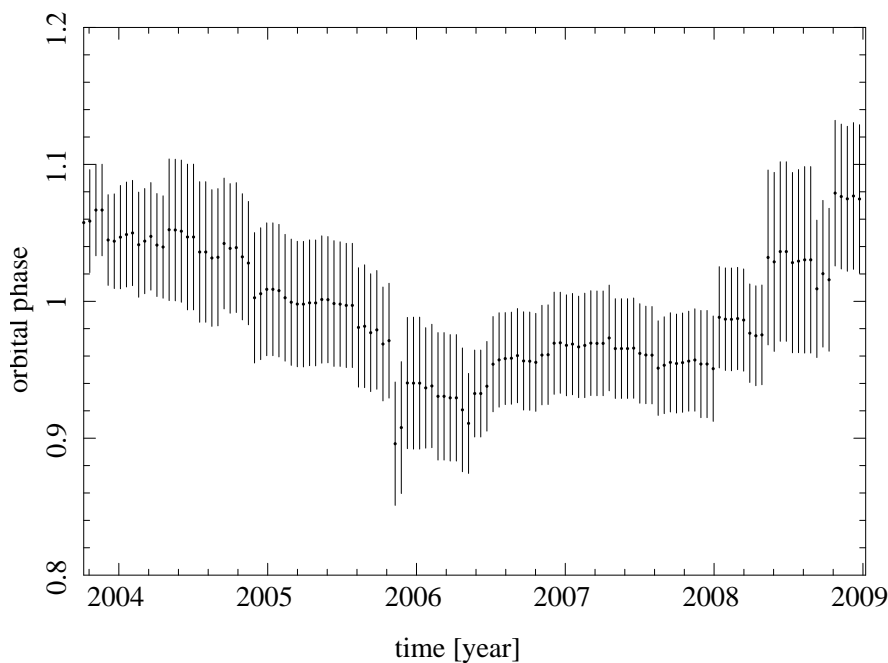


**Figure 4.13:** *Temporal evolution of the center of a two years interval of the dip distribution*

### 4.4.2 Simulated time evolution

To check whether the observed time evolution of the dip distribution is due to selection or statistical effects a Monte Carlo simulation is performed. The null hypothesis is that the measured time evolution of the center of the dip distribution as a function of orbital phase is due to a stable triangular one. To test this, dipoles distributed according to such a distribution are simulated in the following way.

First a triangular distribution is gained by inverse transform sampling (see appendix B). Its parameters are chosen such that the distribution has the maximum at orbital phase 1 and is non-zero from 0.7 to 1.3.

To determine dip occurrence times for the whole time span of the campaign, it is divided into bins of the length of the orbital period. Now a random of these bins is chosen according to a uniform distribution. In this orbital phase bin the dip phase is chosen with the help of the triangular distribution. In this way dipoles are simulated, which are distributed in a triangular shape with respect to the orbital phase.

The measured density of dipoles is 27.92 dipoles per day. For a time span from October 1996 till January 2010 this results in a total number of 135103 dipoles. For one simulation this number of dip occurring times were simulated in the way described beforehand. After that they were filtered with the real observation times to see if there are any selection effects. Hereon the time evolution of the center of the distribution was calculated like for the measured data (see section 4.4.1).

This procedure was repeated 10000 times to calculate a density distribution. The outer black lines in Fig. 4.14 correspond to the maximum and minimum value of the orbital phase of the dip distribution center, whereas 50 % of the simulated time evolutions lie between the inner black lines. The red points correspond to the measured time evolution. It is clearly visible that the measured time evolution differs significantly from the 10000 simulated ones. This leads to the conclusion that the dipoles are not distributed according to a stable triangular distribution. This is an indication for temporal development in the dip occurrence.

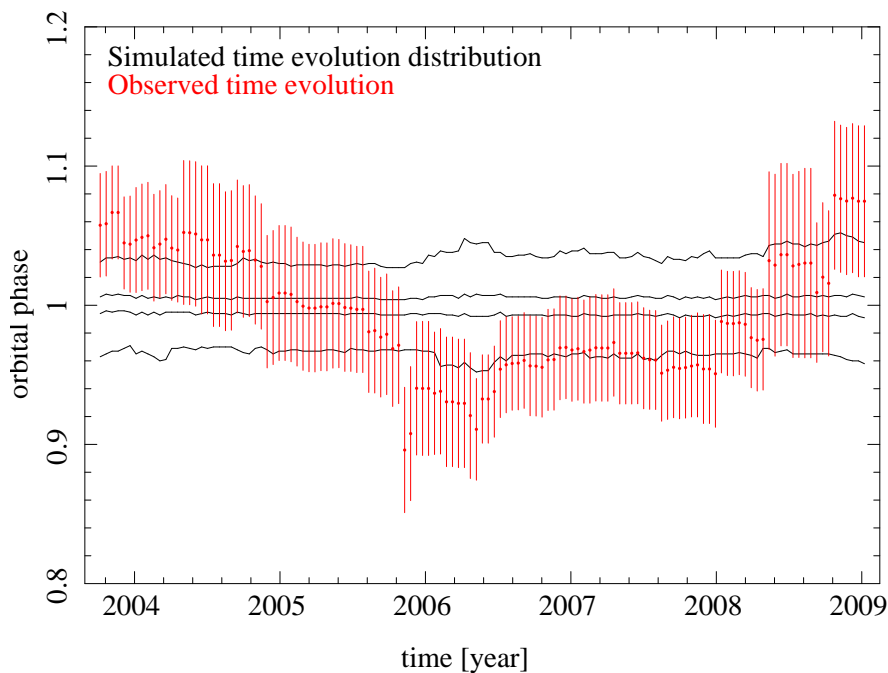


**Figure 4.14:** Density profile of the 10000 simulated time evolutions (black): the outer lines show the maximum and minimum value whereas the inner ones contain 50 % of the data. Measured time evolution (red).

## 4.5 Length distribution

Figure 4.15 shows the dip length distribution. For each dip length the number of dips shorter than this length is plotted. Most dips are at the lower boundary of the criterion with a length of 1 s while the longest dip has a duration of 117 s. It is possible that some of the short time events are due to source variability, but it is difficult to distinguish between absorption dipping and source variability at short time scales. Therefore dipping events shorter than 1 s are excluded from the beginning (see section 3.3). There might be an overestimation of short dips but an objective, formal criterion which is transparent was preferred over the subjective exclusion of dips. However the long timescale events could be clearly identified as dipping events.

It is obvious that longer dips are far more rare than short ones. Looking at some of the longer dips one gets the impression that they have substructures and that there is a possibility that they consist of several shorter dips.

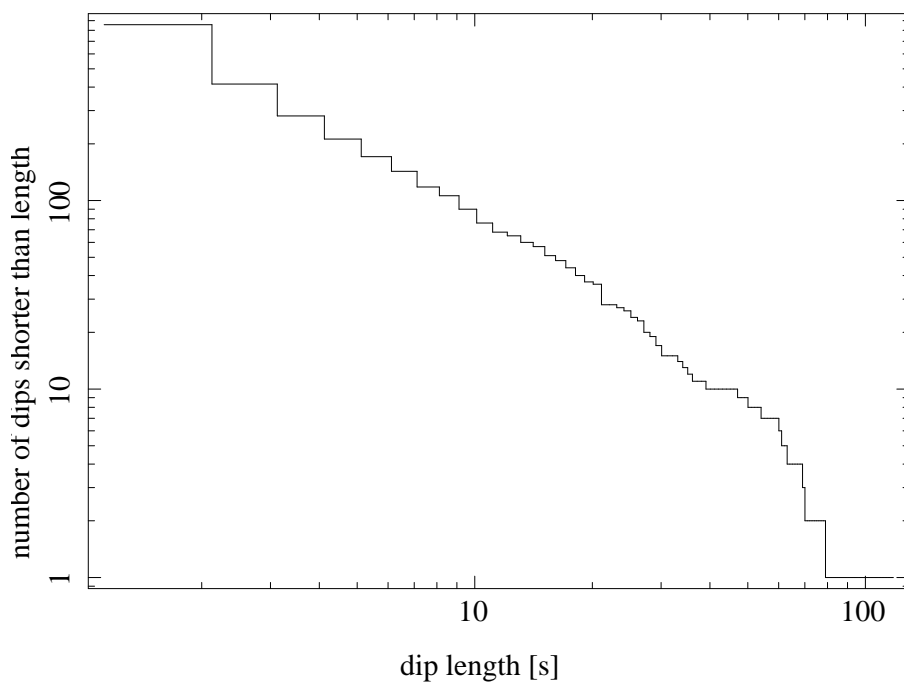


**Figure 4.15:** *Length distribution. Number of dips shorter than respective length.*

To investigate whether long dips consist of shorter ones, the median of the dip length per phase bin was computed. It was tested if there is a correlation between dip length and the occurrence of dips. Such a correlation would strengthen the hypothesis because if there are more dips it should be more probable that they overlap and so build a longer dip. Figure 4.16 shows the comparison between median dip length in the upper panel and dip occurrence in the lower panel. It is clearly visible that the median dip length shows no dependence on the orbital phase whereas the occurrence does. So there is no correlation between the dip length and the occurrence within statistical accuracy.

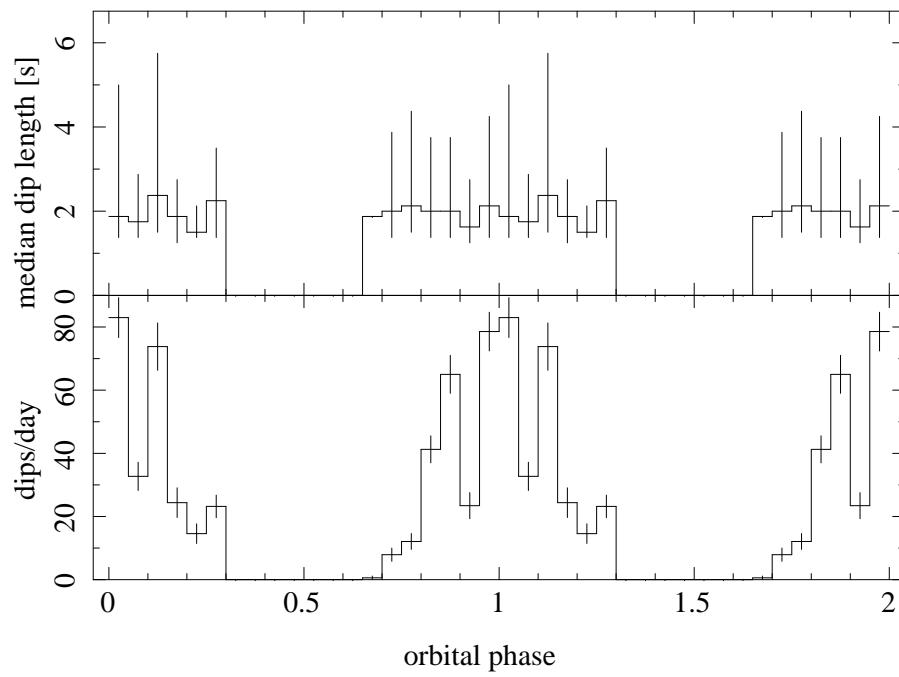


**Figure 4.16:** Median dip length and dip occurrence per phase bin

# Chapter 5

## Summary and outlook

The aim of this work was to study absorption dips in *RXTE* data from Cyg X-1. First a criterion was found based on the deviation of the hardness ratio from the local mean. This criterion turned out to work in the hard state of the source while not only indicating dips during the soft state but also flares and local fluctuations. This observation was tested by using the criterion on simulated light curves which showed that in the hard state only few events are detected because of intrinsic variability while in the soft state this could not be excluded. Therefore only hard state dips were used for further studies.

A distribution of dips in hard state over the orbit was gained. It showed that dips only occur near superior conjunction of the black hole. This is in contrast to the orbital distribution seen in earlier works, where a fixed value for the hardness ratio was used as a criterion and dips were found at all orbital phases. While the distribution seems to be statistically stable it seems to evolve in time. This was emphasized by a Kolmogorov-Smirnov test. This time evolution in the dip distribution was studied further by showing with the help of a Monte Carlo simulation that the dip distribution is most probable not a stable triangular distribution.

Studying the length distribution of dips showed that longer dips which have duration up to 100s are less frequent than shorter ones. There is a possibility that long dips consist of a series of short dips. But there is no evidence for that because no correlation between dip length and occurrence of dips could be found.

To obtain a better understanding of dipping, a criterion which is able to find dips in the soft state in a better way would be helpful. Furthermore the time evolution of the dip distribution should be investigated further as this could yield information about what causes dipping.



# Appendix A

## Two sample Kolmogorov-Smirnov test

To check the stability of the distribution in section 4.3 a two sample Kolmogorov-Smirnov test was performed. With this test the compatibility of two subsets could be checked without knowing the underlying distribution. The null hypothesis is that the cumulative distribution functions  $F_1$  and  $F_2$  of two empiric samples consisting of  $n_1$  and  $n_2$  observations are distributed according to the same distribution. The test statistic is:

$$D = \max \{|F_1(x) - F_2(x)|\}$$

For a discrete sample  $X = \{x_1, x_2, \dots, x_n\}$  it is convenient to use the step function

$$F(x) = \frac{1}{n} |\{y \in X : y \leq x\}|,$$

where  $|Z|$  indicates the number of elements of the set  $Z$ , as the cumulative distribution function. The test statistics is gained by calculating the difference of these functions for the two samples  $D$  at every discrete point  $x \in X_1 \cup X_2$  and calculating the maximum of these values.

The null hypothesis is rejected at level  $\alpha$  if  $D > D_{n_1, n_2, \alpha}$  (see, for example, Sachs, 2006). For  $n_1$  and  $n_2$  large enough  $D_{n_1, n_2, \alpha}$  can be estimated according to:

$$D_{n_1, n_2, \alpha} = \sqrt{\ln\left(\sqrt{\frac{2}{\alpha}}\right)} \cdot \sqrt{\frac{n_1 + n_2}{n_1 n_2}}$$

With the values used in section 4.3,  $n_1 = n_2 = 428$ , and for  $\alpha = 0.01$  we obtain  $D_{428, 428, 0.01} = 0.111$ .

# Appendix B

## Inverse transform sampling

To obtain the triangular distribution which is used in section 4.4.2 inverse transfer sampling was used. This is a method with which a sample distributed according to a given probability distribution  $f_X(x)$  is generated out of a unitary distributed random number  $u \in [0, 1]$ .

The normalized triangular distribution over the periodical phase  $x \in [0, 1]$  with a width of 0.6 and the maximum around 0 respectively 1 is

$$f_X(x) = \begin{cases} \frac{1}{0.3} - \frac{1}{(0.3)^2}x & \text{for } x < 0.3 \\ 0 & \text{for } 0.3 \leq x \leq 0.7 \\ \frac{1}{(0.3)^2}(x - 0.7) & \text{for } 0.7 < x \end{cases},$$

which is plotted in Fig. B.1 on the left side. On the right the cumulative distribution function  $F_X(x)$  is shown which is calculated as

$$F_X(x) = \int_0^x f_X(y) dy = \begin{cases} \frac{x}{0.3} - \frac{x^2}{2 \cdot (0.3)^2} & \text{for } x < 0.3 \\ \frac{1}{2} & \text{for } 0.3 \leq x \leq 0.7 \\ \frac{1}{2} + \frac{1}{2} \left( \frac{0.7}{0.3} \right)^2 + \frac{x^2}{2 \cdot (0.3)^2} - \frac{0.7x}{(0.3)^2} & \text{for } 0.7 < x \end{cases}$$

From which we get the inverse cumulative distribution function

$$F_X^{-1}(u) = \begin{cases} 0.3 - \sqrt{(0.3)^2 - 2u(0.3)^2} & \text{for } u < 0.5 \\ 0.7 + \sqrt{-(1-2u)(0.3)^2} & \text{for } u > 0.5 \end{cases}$$

visible in Fig. B.2. If now  $u$  is chosen as uniformly distributed random variable,  $X = F_X^{-1}(u)$  is distributed according to  $f_X$ . A histogram of an example where 5000 numbers were generated in this way is plotted in Fig. B.2 on the right side.

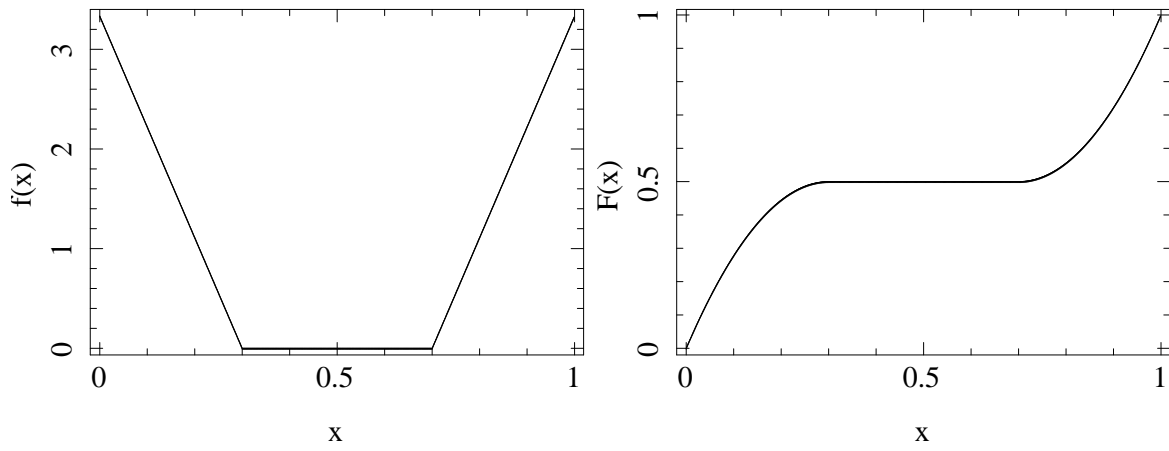


**Figure B.1:** The distribution function  $f_X$  (left) and its cumulative distribution function  $F_X$  (right)

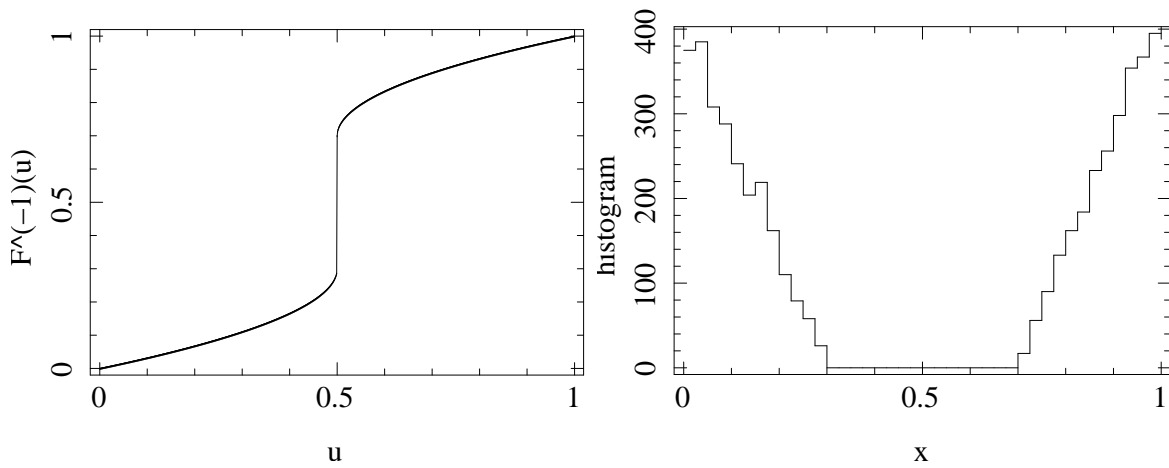


**Figure B.2:** The inverse of the cumulative distribution function  $F_X^{-1}$  (left) and a sample of 5000 numbers generated with the inverse transform sampling method

## Acknowledgments

This work would never have the form it has without the help of the many people I would like to thank. First of all Manfred Hanke who introduced me to the topic, which was rather new for me. From that moment on he was always there when I needed help. Regardless of the question, he always tried to help me the best he could.

I thank Jörn Wilms who spent much of his limited time discussing with me, thinking about my problems and reading what I have written. Furthermore I want to thank Moritz Böck, Christian Schmid, Felix Fürst, Thomas Dauser and Michael Wille for useful discussions and many answers to my questions.

I thank all people at the Remeis observatory who welcomed me into their community with open arms. In the quarter of a year I spent there, it never became boring and always was fun to work there. It was an experience I never will forget and all I have to say in the end is:

Thank you!

# List of Figures

2.1	Schematic drawing of <i>RXTE</i> . . . . .	5
2.2	Expected distribution of clumps in the stellar wind of a massive star . . . . .	6
2.3	Artists impression of the Cygnus X-1 binary system . . . . .	7
2.4	Density profile of the stellar wind with phase dependent line of sight from Earth . . . . .	8
2.5	<i>RXTE</i> -light curve of a dip in the 2–4 keV and 13–15 keV band . . . . .	9
2.6	Chandra spectra without and during the dip . . . . .	10
2.7	Distribution of dips over the orbital phase . . . . .	10
3.1	Monthly exposure . . . . .	13
3.2	Hardness-intensity-diagram . . . . .	13
3.3	Typical dipping event in the hard state . . . . .	14
3.4	Typical type A event in the soft state . . . . .	15
3.5	Typical type B event in the soft state . . . . .	16
3.6	Typical type C event in the soft state . . . . .	17
4.1	Distribution of the hard state dips over the orbit . . . . .	18
4.2	Distribution of the type A/B events and type C events over the orbit . . . . .	19
4.3	Distribution of the dips and <i>RXTE</i> ASM light curve of Cyg X-1 . . . . .	19
4.4	Simulated light curve . . . . .	20
4.5	PSD of a simulated light curve . . . . .	21
4.6	Two light curves simulated with a constant time lag . . . . .	22
4.7	Theoretical distributions of the simulated light curves . . . . .	23
4.8	Two light curves simulated with a frequency dependent time lag . . . . .	24
4.9	Time lag spectrum gained via timing analysis . . . . .	24
4.10	PSDs used for the simulation . . . . .	25
4.11	Subsets of the dip distribution (every other dataset) . . . . .	27
4.12	Subsets of the dip distribution (first/second half) . . . . .	27
4.13	Temporal evolution of the dip distribution . . . . .	28
4.14	Simulated time evolution density . . . . .	29
4.15	Length distribution . . . . .	30
4.16	Median dip length and dip occurrence per phase bin . . . . .	31
B.1	The distribution function and its cumulative distribution function . . . . .	35
B.2	Inverse of the cumulative distribution function and distribution sample . . . . .	35

# List of Tables

3.1	Used PCA-channels and corresponding energy in PCA epoch 5 . . . . .	12
4.1	PSD parameters used for the simulation of light curves . . . . .	25

# Bibliography

- Bałucińska-Church M., Church M.J., Charles P.A., et al., 2000, MNRAS 311, 861
- Bałucińska-Church M., Takahashi T., Ueda Y., et al., 1997, *Astrophys. J., Lett.* 480, L115+
- Boroson B., Vrtilik S., 2010, *ApJ* 710, 197
- Bowyer S., Byram E.T., Chubb T.A., Friedman H., 1965, *Science* 147, 394
- Brocksopp C., Fender R.P., Larionov V., et al., 1999, MNRAS 309, 1063
- Brocksopp C., Fender R.P., Pooley G.G., 2002, MNRAS 336, 699
- Castor J.I., Abbott D.C., Klein R.I., 1975, *ApJ* 195, 157
- Dessart L., Owocki S.P., 2005, *A&A* 437, 657
- Feldmeier A., Oskinova L., Hamann W., 2003, *A&A* 403, 217
- Feng Y.X., Cui W., 2002, *ApJ* 564, 953
- Friend D.B., Castor J.I., 1982, *ApJ* 261, 293
- Fürst F., Kreykenbohm I., Pottschmidt K., et al., 2010, ArXiv e-prints
- Gleissner T., Wilms J., Pooley G.G., et al., 2004a, *A&A* 425, 1061
- Gleissner T., Wilms J., Pottschmidt K., et al., 2004b, *A&A* 414, 1091
- Gruber D.E., Blanco P.R., Heindl W.A., et al., 1996, *A&AS* 120, C641+
- Herrero A., Kudritzki R.P., Gabler R., et al., 1995, *A&A* 297, 556
- Jahoda K., Markwardt C.B., Radeva Y., et al., 2006, *ApJS* 163, 401
- Jahoda K., Swank J.H., Giles A.B., et al., 1996, In: O. H. Siegmund & M. A. Gummin (ed.) *Society of Photo-Optical Instrumentation Engineers (SPIE) Conference Series*, Vol. 2808., p.59
- Kitamoto S., Miyamoto S., Tanaka Y., et al., 1984, *PASJ* 36, 731
- Levine A.M., Bradt H., Cui W., et al., 1996, *Astrophys. J., Lett.* 469, L33+
- Li F.K., Clark G.W., 1974, *Astrophys. J., Lett.* 191, L27
- Nagase F., Hayakawa S., Sato N., et al., 1986, *PASJ* 38, 547
- Nowak M.A., Vaughan B.A., Wilms J., et al., 1999, *ApJ* 510, 874

- Oskinova L.M., Hamann W., Feldmeier A., 2007, *A&A* 476, 1331
- Pottschmidt K., Wilms J., Nowak M.A., et al., 2003, *A&A* 407, 1039
- Poutanen J., Zdziarski A.A., Ibragimov A., 2008, *MNRAS* 389, 1427
- Remillard R.A., McClintock J.E., 2006, *ARA&A* 44, 49
- Rothschild R.E., Blanco P.R., Gruber D.E., et al., 1998, *ApJ* 496, 538
- Sachs L., 2006, *Einführung in die Stochastik und das stochastische Denken*, Harri Deutsch
- Sako M., Liedahl D.A., Kahn S.M., Paerels F., 1999, *ApJ* 525, 921
- Shaposhnikov N., Titarchuk L., 2007, *ApJ* 663, 445
- Timmer J., Koenig M., 1995, *A&A* 300, 707
- Vaughan B.A., Nowak M.A., 1997, *Astrophys. J., Lett.* 474, L43+
- Walborn N.R., 1973, *Astrophys. J., Lett.* 179, L123+
- Watanabe S., Sako M., Ishida M., et al., 2006, *ApJ* 651, 421
- Wilms J., Nowak M.A., Pottschmidt K., et al., 2006, *A&A* 447, 245



# Declaration

Hereby I declare that I wrote this bachelor thesis autonomously and that I have not used other resources than those quoted in this work.

# Erklärung

Hiermit bestätige ich, dass ich diese Arbeit selbstständig und nur unter Verwendung der angegebenen Hilfsmittel angefertigt habe.

Erlangen,

Eckhard Strobel